Diffuse elastic wavefield within a simple crustal model. Some consequences for low and high frequencies

Antonio García-Jerez[1], Francisco Luzón[1,2], Francisco J. Sánchez-Sesma[3], Enrico Lunedei[4], Dario Albarello[4], Miguel A. Santoyo[5], Javier Almendros[1]

[1] IAGPDS, Campus Universitario de Cartuja, Universidad de Granada, 18071 Granada, Spain. Corresponding author: A. G.-J., email: agjerez@ugr.es

[2] Departamento de Química y Física, Universidad de Almería, 04120 La Cañada, Almería, Spain.

[3] Instituto de Ingeniería, Universidad Nacional Autónoma de México, CU, Coyoacán, 04510 D.F., Mexico.

[4] Dipartimento di Scienze Fisiche, della Terra e dell'Ambiente, Università degli Studî di Siena, Via Laterina 8, 53100 Siena, Italy.

[5] Departamento de Física de la Tierra, Universidad Complutense de Madrid, Madrid, Spain.

Submitted to Journal of Geophysical Research

Revised version. October 2013.

This article has been accepted for publication and undergone full peer review but has not been through the copyediting, typesetting, pagination and proofreading process which may lead to differences between this version and the Version of Record. Please cite this article as doi: 10.1002/2013JB010107

KEY POINTS

Expressions for power spectra of diffuse fields in a layered halfspace are found

High-frequency ambient noise coherences are studied for a simple crustal model

Ambient noise H/V ratio on rock is experimentally and theoretically investigated

ABSTRACT

The reliability of usual assumptions regarding the wavefield composition in applications of the Diffuse Field Approach (DFA) to passive seismic prospecting is investigated. Starting from the more general formulation of the DFA for full wavefield (FW), the contribution of each wave to the horizontal- and vertical-component power spectra at surface are analyzed for a simple elastic waveguide representing the continental crust - upper mantle interface. Special attention is paid to their compositions at low- and high-frequencies, and the relative powers of each surface wave (SW) type are identified by means of a semi-analytical analysis. If body waves are removed from the analysis, the high-frequency horizontal asymptote of the H/V spectral ratio decreases slightly (from 1.33 for FW to around 1.14 for SW) and shows dependence on both the Poisson's ratio of the crust and the S-wave velocity contrast (while FW-H/V asymptote depends on the former only). Experimental tests in a local broad-band network provide H/V curves compatible with any of these values in the band 0.2 - 1 Hz, approximately, supporting the applicability of the DFA approximation. Coexistence of multiple SW-modes produces distortion in the amplitudes of vertical and radial-component Aki's coherences, in comparison with the usual predictions based on fundamental modes. At high frequencies, this effect consists of a decrement by a constant scaling factor, being very remarkable in the radial case. Effects on the tangential coherence are severe, including a $-\pi/4$ phase shift, slower decay rate of amplitude vs. frequency and contribution of several velocities for large enough distances.

INDEX TERMS

Surface waves and free oscillations, Theory, Body waves, Continental crust.

1. INTRODUCTION

The possibility of retrieving the approximate elastodynamic Green's tensor between two stations embedded in an elastic medium from averaged time-domain cross-correlation of their ambient noise records was confirmed in seismic experiments by *Shapiro and Campillo* [2004]. After those pioneering results, several theoretical works on this subject have been conducted for simple models [e.g., *Sánchez-Sesma and Campillo,* 2006; *Sánchez-Sesma et al.,* 2006 and 2008], showing that such a possibility exists under the condition of diffuse wavefield, implying that isotropy of illumination and certain relationships between the energies of different types of waves (derived from the energy equipartition principle) have to be fulfilled.

These ideas, which are generically called seismic interferometry, have been extensively used for imaging the surface-wave velocity structure in vast regions across the world by using long recording time (often several years) and large permanent broadband seismic networks. In addition, the technique has permitted to invert structural models of the crust and upper-mantle in terms of S-wave velocity. That obtained by *Yao et al.* [2008] at SE Tibet for depths down to about 100 km is an example of this. Recently, *Pawlak et al.* [2011] have prospected the structure beneath Hudson Bay (North America) obtaining several 1D models down to 80 km depth, while *Luo et al.* [2012] have inverted a 3D model of the Dabie orogenic belt structure (China) down to 45 km. Most of these studies rely on interpretation of single-mode dispersion curves retrieved from low frequency cross-correlations. Only some works [e.g.,

Nishida et al., 2008] include discussion of higher modes.

The close relation between the well-known Aki's Spatial Autocorrelation method (SPAC) [*Aki*, 1957], formulated in frequency domain, and seismic interferometry, typically implemented in time domain, has been investigated by *Yokoi and Margaryan* [2008]. Basically, diffuse field hypotheses are more stringent than the requisites of the SPAC method, because they fix the relative contributions of different types of surface waves, which were treated as unknowns in the original implementation of SPAC. Moreover, Aki's method states a meaningful way for normalization of cross-correlations, by using power spectral densities. Predominance of fundamental modes in horizontal and vertical components is assumed in the majority of the applications of SPAC and SPAC-like methods [e.g., *Ferrazzini et al.*, 1991; *Métaxian and Lesage*, 1997; *Bettig et al.*, 2001; *Köhler et al.*, 2007], although a method for combining different modes, in order to construct an effective or apparent dispersion curve, has been explained, e.g., in *Tokimatsu* [1997]. Different aspects of these techniques were discussed by *Chávez-García and Luzón* [2005].

A simpler operative method for obtaining information about the geological structure from single-station records in the framework of diffuse wavefield theory has been developed by *Sánchez-Sesma et al.* [2011a]. It is based on the interpretation of the Nakamura's H/V spectral ratio [*Nakamura*, 1989] in terms of full-wavefield Green's functions. Assuming that a 3D diffuse, equipartitioned displacement vector field $u_i(\mathbf{x},t)$ is established within an elastic medium with a bounded heterogeneous region, the power spectral densities of motions at point $\mathbf{x}$ along the direction *m* can be obtained as [*Sánchez-Sesma et al.*, 2008]:

$$P_m(\mathbf{x},\omega) \equiv \lim_{\tau\to\infty} \frac{\left\langle u_m(\mathbf{x},\omega;\tau) u_m^*(\mathbf{x},\omega;\tau)\right\rangle}{\tau} = -2\pi\omega^{-1}\rho\beta^3 S^2 \,\mathrm{Im}[G_{mm}(\mathbf{x};\mathbf{x};\omega)], \text{ no sum,} \quad (1)$$

where $G_{ij}(\mathbf{x_A},\mathbf{x_B},\omega)$ is the Green's tensor between $\mathbf{x_B}$ and $\mathbf{x_A}$, $\omega = 2\pi f$ the circular frequency, ρ and β the mass density and the shear wave propagation velocity in the homogeneous space, S^2, with dimensions L^2T, the average power spectral density of shear wave displacements, which is a measure of the strength of the diffuse illumination and τ represents the length of a time window applied to the stationary records before Fourier transforming. It is assumed that this representation can be extended to a layered structure, with ρ and β interpreted as halfspace properties [*Sánchez-Sesma et al.*, 2011a]. Thus, the total energy per unit volume in the band $[f \quad f+df]$, at a point $\mathbf{x}$, $2\rho(\mathbf{x})\omega^2 \sum_m P_m(\mathbf{x},\omega)df$, $f > 0$, is proportional to the imaginary part of the trace of the Green's tensor for coincident receiver and source. In general, the imaginary part of, say, G_{11} is proportional to the power injected by a unit harmonic load in direction 1. This quantity "detects" energies that are both radiated and coming back to the source and may be used for imaging. Finally, we can thus write the H/V ratio as:

$$[H/V](\omega) \equiv \sqrt{\frac{P_1+P_2}{P_3}} = \sqrt{\frac{2\,\mathrm{Im}[G_{11}(\mathbf{x};\mathbf{x};\omega)]}{\mathrm{Im}[G_{33}(\mathbf{x};\mathbf{x};\omega)]}}\,. \quad (2)$$

Equation (2) links average measurements expressed on the left side with an intrinsic property of the medium on the right, and naturally allows for inversion of H/V ratios accounting for the contributions of Rayleigh, Love and body waves. Right hand side of Eq. (2) relies on the assumption of depth-dependent medium properties (horizontal layering), for which horizontal directions are indistinguishable (*i. e.*, $P_1 = P_2 = P_H/2$ and generally different from $P_3 = P_V$).

An alternative scheme for calculation of H/V ratios in diffuse wavefields based on the spectral decomposition of the elastic wave operator has been developed by *Margerin* [2009] and *Margerin et al.* [2009].

On the basis of this formulation, and taking into account the classical representation of the Green's tensor in a layered medium as an integral on the complex-*k* plane, separate formulae for body-, Rayleigh- and Love-wave components of P_H and P_V are given. The low- and high-frequency behavior of P_H, P_V and H/V are subsequently analyzed for the case of a simple waveguide by using Harkrider's nomenclature for the modal contributions of surface waves. Then, the immediate consequences for a simple model of a layer overlying a halfspace, which approximates the continental crust over the upper mantle, are explored and tested with experimental data. Finally, asymptotic forms for the three Aki's spatial autocorrelation coefficients (coherences) [*Aki*, 1957] are derived and successfully tested by means of numerical experiments. An important result is the major role played by higher Rayleigh and Love modes in the high-frequency wavefield. The effects of these waves on power spectra, spectral ratios and coherences are discussed in detail.

2. HORIZONTAL AND VERTICAL POWER SPECTRA IN A PLANE LAREYED ELASTIC MEDIUM

For several decades, extensive efforts have been devoted to developing suitable methods for calculation of the Green's functions in a layered medium. Regardless of its eventual problems of stability, which can be properly circumvented, we will rely on a straightforward generalization to full wavefields of the Harkrider's formulation [*Harkrider*, 1964] for a layered medium with *j*-th layer properties α_j (*P*-wave velocity), β_j (*P*-wave velocity), ρ_j (density), d_j (thickness, $j = 1, 2, \ldots N$ increasing downwards, and $d_N = \infty$ for the halfspace)

as starting point of this research.

In this manner, the displacements for a surface point force and a shallow receiver at distance r, can be expressed by means of integrals on the horizontal wavenumber of Bessel's functions $J_n(kr)$ with kernels

$$f_{PSV}^{V}(k) = -\frac{[GN - LH]}{[NK - LM]},\ f_{PSV}^{H}(k) = \frac{[RM - SK]}{[NK - LM]},\ f_{SH}(k) = \frac{(J_L)_{12} - (J_L)_{22}}{(J_L)_{21} - (J_L)_{11}} \tag{3}$$

depending of quantities G, H, J_L, K, L, M, N, R, S defined e.g., by *Harkrider* [1964]. Hereafter, only the imaginary parts of three components of the Green's tensor will be needed, namely, i) the vertical displacement at distance r due to a vertical force (assumed to be at the origin), which can be represented in cylindrical coordinates as $\mathrm{Im}[G_{zz}(r,\theta;0;\omega)]$ at z = 0; ii) the radial displacement generated by a horizontal force at a point located on the force direction, $\mathrm{Im}[G_{rr}(r,\theta;0,\theta;\omega)]$; and iii) the motion parallel to a horizontal force, at a point located on its perpendicular direction, $\mathrm{Im}[G_{\theta\theta}(r,\theta;0,\theta;\omega)]$. Considering the axial symmetry of the medium, the receiver can be assumed to have any particular azimuth, e.g., to lay on the x_1 axis (θ = 0) at $x_1 = r$, so that $G_{rr}(r,0;0,\theta;\omega)$ and $G_{\theta\theta}(r,0;0,\theta;\omega)$ can be rewritten in Cartesian coordinates as $G_{11}(r,0,0;0;\omega)$ and $G_{22}(r,0,0;0;\omega)$.

Since their integrands present simple poles on the real-k axis associated to surface waves, the respective integral forms,

$$\mathrm{Im}[G_{33}(r,0,0;0;\omega)] = \mathrm{Im}\left[\frac{\mathrm{i}}{2\pi}\int_0^{+\infty} f_{PSV}^{V}(k)J_0(kr)dk\right], \tag{4}$$

$$\mathrm{Im}\left[G_{11}(r,0,0;0;\omega)\right] = \mathrm{Im}\left[\underbrace{\frac{\mathrm{i}}{4\pi}\int_0^{+\infty} f_{SH}(k)\left[J_0(kr)+J_2(kr)\right]dk}_{SH} + \underbrace{\frac{\mathrm{i}}{4\pi}\int_0^{+\infty} f_{PSV}^{H}(k)\left[J_0(kr)-J_2(kr)\right]dk}_{PSV}\right], \quad (5)$$

$$\mathrm{Im}\left[G_{22}(r,0,0;0;\omega)\right] = \mathrm{Im}\left[\underbrace{\frac{\mathrm{i}}{4\pi}\int_0^{+\infty} f_{SH}(k)\left[J_0(kr)-J_2(kr)\right]dk}_{SH} + \underbrace{\frac{\mathrm{i}}{4\pi}\int_0^{+\infty} f_{PSV}^{H}(k)\left[J_0(kr)+J_2(kr)\right]dk}_{PSV}\right], \quad (6)$$

can be better evaluated by using the Cauchy's residues theorem for a suitable integration contour such as that shown in Fig. 1 [e.g., *Tamura*, 1996]. Apart from the poles, the integrands show branch-cut discontinuities in the interval $[-\omega/\beta_N, +\omega/\beta_N]$ and along the whole imaginary axis due to the dependence on the square roots $\nu_{\alpha_N} = \sqrt{k^2 - (\omega/\alpha_N)^2}$ and $\nu_{\beta_N} = \sqrt{k^2 - (\omega/\beta_N)^2}$. The criteria used in this section for definition of Fourier transform and signs of ν_{α_j} and ν_{β_j} are parallel to those in *Aki and Richards* [2002]. Some details about integration for an arbitrary *r* (not required here) can be found in *Tamura* [1996] and *Wang and Herrmann*, [1980]. Note that dealing with horizontal components for *r*>0 would entail specific treatment of the poles at *k* = 0 generated when Bessel functions $J_2(kr)$ in (5-6) are rewritten in terms of Hankel functions $H_2^{(1)}(\pm kr)$ [see *Wang and Herrmann*, 1980]. Function $J_0(kr)$ does not produce this type of singularities.

Derivation of suitable expressions for the contributions of different types of waves to the diffuse-field power spectra at surface may be started taking the limit $r \rightarrow 0$ in the previous formulae. Nevertheless, in order to avoid numerical instability due to divergence in the real

parts of the Green's functions for coincident source and receiver, only those terms contributing to their imaginary part will be preserved and evaluated. Separation of the Green's function expressions into their real and imaginary parts can be naturally achieved by using the suggested contour integral. First of all, it should be noted that terms in (5-6) containing $J_2(kr)$ vanish for $r \to 0$ due to the zero limit of this Bessel function. Consequently, they can be disregarded hereafter and the mentioned precautions concerning possible poles at $k = 0$ can be ignored.

Taking into account that $f_{PSV}^{V}(k)$, $f_{PSV}^{H}(k)$ and $f_{SH}(k)$ are odd functions of k, the integrals can be extended to the whole real axis replacing $J_n(kr)$ with $H_n^{(1)}(kr)/2$ and subsequently interpreted in the complex-k plane taking advantage of the integration contour. In this manner, the original integrals are evaluated from the sum of residues (corresponding to Rayleigh and Love waves) and the branch-cut integrals in $[0, \omega/\beta_N]$ and [0,+i∞) (corresponding to body waves). Nevertheless, due to the conjugation of $f_{PSV}^{V}(k)$, $f_{PSV}^{H}(k)$ and $f_{SH}(k)$ between both sides of the imaginary axis, integration in the latter interval will contribute to the real part of the Green's function only. For a generic $f(k)$ fulfilling the mentioned properties, the useful result is [e.g., *Tamura,* 1996]:

$$\int_0^{+\infty} f(k) J_0(kr)\,dk = i\pi \sum_m \text{Residue}[f(k)]_{k=k_m} H_0^{(1)}(k_m r) + \int_0^{k_{\beta_N}} \text{Re}\left[f(k)\right]_{4^{th}} H_0^{(1)}(kr)\,dk$$

$$-i\frac{2}{\pi}\int_0^{+\infty} \text{Im}\left[f(ik)\right]_{2^{nd}} K_0(kr)\,dk\,, \qquad (7)$$

where m runs over the poles of $f(k)$ and subscripts 4th and 2nd are specifying the quadrant

used for evaluation of ν_{α_j} and ν_{β_j}. Using (7) in Eqs. (4-5) and taking the limit $r \to 0$, we finally obtain:

$$\mathrm{Im}[G_{33}(0;0;\omega)] = -\frac{1}{2}\sum_{m\in\mathrm{RAYLEIGH}} A_{Rm} + \frac{1}{2\pi}\int_0^{\omega/\beta_N} \mathrm{Re}\left[f_{PSV}^{V}(k)\right]_{4^{th}qu} dk\,, \tag{8}$$

$$\mathrm{Im}[G_{11}^{PSV}(0;0;\omega)] = \mathrm{Im}[G_{22}^{PSV}(0;0;\omega)] = -\frac{1}{4}\sum_{m\in\mathrm{RAYLEIGH}} A_{Rm}\chi_m^2 + \frac{1}{4\pi}\int_0^{\omega/\beta_N} \mathrm{Re}\left[f_{PSV}^{H}(k)\right]_{4^{th}qu} dk\,, \tag{9}$$

$$\mathrm{Im}[G_{11}^{SH}(0;0;\omega)] = \mathrm{Im}[G_{22}^{SH}(0;0;\omega)] = -\frac{1}{4}\sum_{m\in\mathrm{LOVE}} A_{Lm} + \frac{1}{4\pi}\int_0^{\omega/\beta_N} \mathrm{Re}\left[f_{SH}(k)\right]_{4^{th}qu} dk\,, \tag{10}$$

where A_{Rm} and A_{Lm} are the medium responses for the *m*-th Rayleigh and Love modes [*Harkrider*, 1964] and χ_m is the ellipticity of the *m*-th Rayleigh mode. Note that numerical integration is constrained to the range $[0, \omega/\beta_N]$. The separate calculation of surface and body waves will be useful for the subsequent analysis.

3. LOW- AND HIGH-FREQUENCY STRUCTURE OF P_H AND P_V IN A SIMPLE WAVEGUIDE

3.1 Low-frequency behavior

It is well known that, in the low frequency limit, our layered structure behaves as semi-infinite medium with the properties of the original model's halfspace [e.g., *Buchen and Ben-*

Hador, 1996, pp. 874]. Thus, we may rely on the Weaver`s calculations of energy partitions between Rayleigh and body waves [*Weaver*, 1985], shown in Fig. 2. A review on this issue has been recently published by *Sánchez-Sesma et al.* [2011b].

In particular, the convergence of the H/V ratio for surface waves (SW) to the fundamental-mode ellipticity can be easily verified from Eqs. (8-10) taking the trends of A_{L0} and A_{R0} as the wavenumbers approach zero into account. Specifically, it can be shown that $A_{L0} \propto k_{L0}^2$ as $k_{L0} \rightarrow 0$ and $A_{R0} \propto k_{R0}$ as $k_{R0} \rightarrow 0$ [e.g., *Harkrider*, 1970], where k_{Rm} (k_{Lm}) is the wavenumber of the *m*-th Rayleigh (Love) mode at a given frequency, implying dominance of the fundamental Rayleigh mode (i. e. $A_{L0}/\left(A_{R0}\chi_0^2\right) \rightarrow 0$ as $\omega \rightarrow 0$, since k_{R0}/k_{L0} tends to a finite positive limit). As a consequence of this fact and of the absence of higher modes at low frequencies, the H/V ratio for SW, $\sqrt{(A_{R0}\chi_0^2 + A_{L0})/A_{R0}}$, is controlled by the fundamental-mode ellipticity, χ_0, which, for $\omega \rightarrow 0$, tends to its value for a semi-infinite medium with properties α_N, β_N, say $\chi_{HS}(\alpha_N, \beta_N)$:

$$\chi_0(f) \rightarrow \chi_{HS}(\alpha_N, \beta_N) = \frac{2\text{-}V_N^2/\beta_N^2}{2\sqrt{1\text{-}V_N^2/\alpha_N^2}}, \text{ as } \omega \rightarrow 0 \qquad (11)$$

[e.g., *Ben-Menahem and Singh*, 2000, equation 3.109]. V_j stands for the Rayleigh wave velocity in a halfspace with *j*-th layer properties. Note that χ_{HS} can be also rewritten as a function of the Poisson's ratio ν_N (Fig. 2c).

3.2 High frequency behavior

Although total (or full-wave, FW) powers P_H and P_V, and consequently the H/V ratio, asymptotically converge at high frequency to those of a halfspace with the Poisson's ratio of the upper layer (Fig. 2), their partitions among different types of waves are more complicated, due to existence of multiple surface-wave modes. In fact, both Rayleigh and Love waves may represent major contributions to the total powers and, moreover, their energies are given by the sum of the contributions of numerous propagation modes.

The high-frequency behaviors of the SW sums $\sum_m A_{Lm}$, $\sum_m A_{Rm}$ and $\sum_m A_{Rm}\chi_m^2$ are studied below. The joint asymptotic trend of the body waves (BW) components can be calculated by subtraction from the FW results. As shown, the fundamental mode of Love waves does not play any special role in the total power. On the contrary, the fundamental Rayleigh mode does carry a significant part of the energy itself.

3.2.1 Love waves at high frequencies

In this case of a single layer (N=2), function $A_{Lm}(f)$ emerges at the m-th mode cutoff frequency and tends to a common horizontal asymptote as f increases. For increasing values of m, $A_{Lm}(f)$ presents steeper transitions to the constant behavior, tending to a (rescaled and translated) Heaviside's function for infinite m. That finite high-frequency limit [*Harkrider*, 1970] is the same for any mode and depends on the upper layer thickness d_1 and shear modulus μ_1:

$$A_{Lm}(f \to \infty) = \frac{1}{\mu_1 d_1} = \frac{1}{\rho_1 \beta_1^2 d_1}. \tag{12}$$

An example of this behavior for a simple model representing the continental crust [*Gilbert*,

1964], listed in Table 1 (Model 1), is shown in Fig. 3. Since the number of active modes (say n) grows proportionally to the frequency whereas the number of modes for which A_{Lm} is significantly different from the asymptote remains bounded, a behavior $\sum_m A_{Lm}(f) \cong n(f)A_L(\infty) \propto f$ is expected (dot-dashed line in Fig. 3). From the well-known expression of the cutoff frequencies of Love modes [e.g., *Ben-Menahem and Singh*, 2000] we finally find that $\sum_m A_{Lm}(f)$ presents an oblique asymptote with slope, a_L, given by:

$$a_L = \lim_{f->\infty} \frac{1}{f} n(f) A_L(\infty) = \frac{2\sqrt{\beta_2^2/\beta_1^2 - 1}}{\rho_1 \beta_1^2 \beta_2} \quad . \tag{13}$$

3.2.2 Rayleigh waves at high frequencies

It is well known that, in the case of a single layer over a half-space, two different subcases can be distinguished in the resolution of Rayleigh wave dispersion equation depending on the relation between the phase velocity c and α_1 [e.g., *Ben-Menahem and Singh*, 2000, pp. 118-119]. For simplicity, we will restrict our attention to models for which $\alpha_1 > \beta_2$ (implying $c < \alpha_1$) such as the simple crustal models discussed in this paper. Unlike Love-wave modes, fundamental and higher Rayleigh modes play different roles in both P_H and P_V. In particular, A_{R0} grows proportionally to f at high frequencies, with a limit of $A_{R0}(f)/f$ calculable in terms of a halfspace with top layer properties, whereas medium responses for higher modes are decreasing functions as f increases towards infinity: $A_{Rm}(f) \propto (m^2/f^2)$ for $m > 0$. In spite of this decaying behavior for any particular higher mode, the superposition $\sum_{m>0} A_{Rm}(f)$ grows proportionally to f, being non-negligible when compared with A_{R0}. Rayleigh medium responses for Model 1 are shown in Fig. 4. Results of the quantitative analysis can be summarized as follows.

The high-frequency behavior of $A_{R0}(f)$ corresponds to an oblique asymptote with slope a_{R0}^V given by the expression:

$$a_{R0}^V = \lim_{f->\infty} \frac{k_{R0}}{f} \frac{A_{R0}}{k_{R0}} = \frac{2\pi}{V_1} \lim_{f->\infty} \frac{A_{R0}}{k_{R0}} =$$

$$= \frac{\pi\sqrt{1-V_1^2/\alpha_1^2}}{2\rho_1 V_1^3\left[(1-\gamma_1)+\left(\frac{\beta_1\gamma_1}{V_1\,\alpha_1(\gamma_1\text{-}1)}\right)^2\left(\alpha_1^2+\beta_1^2-2V_1^2\right)\right]}, \qquad (14)$$

where $\gamma_1 = 2\beta_1^2/V_1^2$ [*Harkrider*, 1970]. Quantity a_{R0}^V plays an important role in the high frequency trend of P_V, and it has to be multiplied by the squared ellipticity $\chi_{HS}^2(\alpha_1,\beta_1)$ (given by Eq. 11 with N replaced by 1) to obtain its counterpart for P_H:

$$a_{R0}^H = \chi_{HS}^2 a_{R0}^V = \frac{\pi\left(2-V_1^2/\beta_1^2\right)^2}{8\rho_1 V_1^3\sqrt{1-V_1^2/\alpha_1^2}\left[(1-\gamma_1)+\left(\frac{\beta_1\gamma_1}{V_1\,\alpha_1(\gamma_1\text{-}1)}\right)^2\left(\alpha_1^2+\beta_1^2-2V_1^2\right)\right]}. \qquad (15)$$

The high-frequency behavior of the set of higher modes can be studied in a semi-analytical way as shown in Appendix A. The slopes of $\sum_{m>0} A_{Rm}(f)$ and $\sum_{m>0} A_{Rm}(f)\chi_m^2(f)$ at high frequencies can be computed as:

$$a_{R\,high}^V = \lim_{f\to\infty}\frac{1}{f}\sum_{m>0} A_{Rm}(f) = \frac{2d\sqrt{\beta_2^2/\beta_1^2-1}}{\beta_2}\int_0^1 d\xi A_{R\infty}[\pi\sqrt{\frac{\beta_2^2}{(\beta_2^2\text{-}\beta_1^2)\xi^2}-1}] \qquad (16)$$

and

$$a^{H}_{R\,high} = \lim_{f\to\infty} \frac{1}{f} \sum_{m>0} \chi^2_m(f) A_{Rm}(f)$$

$$= \frac{2d\sqrt{\beta_2^2/\beta_1^2 - 1}}{\beta_2} \int_0^1 d\xi \chi^2_\infty [\pi \sqrt{\frac{\beta_2^2}{(\beta_2^2\text{-}\beta_1^2)\xi^2} - 1}] A_{R\infty} [\pi \sqrt{\frac{\beta_2^2}{(\beta_2^2\text{-}\beta_1^2)\xi^2} - 1}], \qquad (17)$$

respectively, where $A_{R\infty}[\cdot]$ and $\chi_\infty[\cdot]$ represent the medium response and ellipticity of a very high order mode ($m \to \infty$) as a function of k_{Rm}/m. Shapes of $A_{R\infty}[\cdot]$ and $\chi_\infty[\cdot]$ for Model 1 have been represented with thick black lines in Fig 5 together with the shapes of A_{Rm} and χ_m functions for the first 70 higher modes. As shown, only a few curves corresponding to low-order higher modes present substantial differences from the limit one. These integral expressions can be numerically estimated (by using a small enough step in ξ) without any problem of stability.

4. HIGH-FREQUENCY H/V FOR THE EARTH'S CRUST

We subsequently explore the possibility of explaining in this way the high-frequency trends of experimental H/V ratios for ambient noise, on the basis of the simple continental crust model listed above (Model 1). The theoretical FW-, BW- and SW-H/V ratios for this structure, according to Eqs. (2) and (8-10), are shown in Fig. 6c. The frequency of the main peak in the FW curve (20 mHz) approximates maxima of Rayleigh wave ellipticity obtained from more detailed models of continental crust and mantle [e.g., *Harkrider*, 1970, Table 5]. At higher frequencies, the oscillatory behavior of decreasing amplitude shows absolute fluctuations in FW-H/V of ±0.05 at 0.1 Hz, ±0.01 at 0.5 Hz and ±0.005 at 1 Hz,

approximately, which can be disregarded in comparison with typical experimental uncertainties (of about ±0.1 in our experiments). Thus, constant H/V ratios can be considered for comparison with experimental data from about 0.1 Hz. The high frequency asymptotes for all SW- and FW- curves have been shown in Fig. 6 with dashed black lines. Calculations for SW follow Sections 3.2.1-2, whereas the asymptotes of FW- P_H and P_V and the high-frequency limit of FW-H/V (~ 1.329) have been taken from Fig. 2 considering the upper-layer Poisson`s ratio. Note that convergence at high frequencies to the halfspace behavior does not hold for all individual types of waves in P_H or P_V, since Love and higher Rayleigh modes do not exist in a half-space. Even so, power vs. frequency curves present oblique asymptotes for all wavefield components.

Assuming a perfectly diffuse wavefield at high frequencies and using the expressions found in Section 3, we find that 39.0% of horizontal motion energy would be carried by body waves and 61.0 % by surface waves, which, in turn, should consist of 68.3% of Love waves, 29.1% of fundamental-mode Rayleigh waves and 2.6% of higher modes of Rayleigh waves (Fig. 6a). Vertical component would be widely dominated by Rayleigh waves (82.4%) with the fundamental mode representing the 81.8% of their power (67.4% of P_V, Fig. 6b). The high-frequency H/V presents a more complex behavior when it is restricted to SW. The limit can be evaluated as

$$\left[H/V\right]_{SW}(\infty) = \sqrt{\frac{2\lim\limits_{f\to\infty} P_H^{SW}(f)/f}{\lim\limits_{f\to\infty} P_V^{SW}(f)/f}} = \sqrt{\frac{a_L + a_{R0}^H + a_{R\,high}^H}{a_{R0}^V + a_{R\,high}^V}}\ , \tag{18}$$

where the slopes have been computed in Eqs. (13-17), leading to a value of 1.143 for Model 1 (Fig. 6c). In particular, the results of (18) show significant dependence on both the upper

layer Poisson's ratio and the S-wave velocity contrast. In other words, $[H/V]_{SW}(\infty)$ preserves some information about the deeper structure through the terms $a^{V}_{R\,high}$ (Eq. 16) and $a^{H}_{R\,high}$ (Eq. 17), whereas a_L, a^{H}_{R0} and a^{V}_{0} depend only on the upper stratum properties. The actual capability of $[H/V]_{SW}(\infty)$ for constraining the crustal model can be simply investigated by means of a representation of its sensitivity to variations in the model parameters. As shown in Fig. 7a-b, this quantity is sensitive to both the S-wave velocity ratio β_2/β_1 and the α_1/β_1 ratio (or to the Poisson's ratio of the upper layer), increasing as any of these quantities increases. The derivatives $\left|x\,\partial[H/V(\infty)]_{SW}/\partial x\right|$, which measure the capability for detecting relative variations in *x* from variations in $[H/V]_{SW}(\infty)$ are shown in Figs. 7c-d. They yield 0.26 for $x=\alpha_1/\beta_1$ and 0.16 for $x=\beta_2/\beta_1$, for variations around the crustal Model 1, highlighting the stronger dependence on the former one in spite of the non-negligible sensitivity to the latter (and consequently, to deep medium characteristics).

For illustration purpose, we have applied the H/V method to ambient noise records obtained at five stations of the University of Almería Network in the western Pyrenean edge, all of them located on hard rock (Table 2) and installed in subsurface vaults. The dataset consisted of broad-band ambient noise waveforms recorded by Guralp-3ESPDC seismometers. The sampling rate was 100 Hz, and the minimum recording time used was 7 months. Power spectra of each component were calculated for one hour long windows, subsequently normalized by the total kinetic energy of the window, and stacked over the set of segments to obtain a daily estimate. The overall shape of the average experimental curves (gray lines in Fig. 8f) presents a decreasing trend from high amplitudes (6 to 13) around 20 mHz to values below 2 at about 0.1 Hz and remains ranging between 1 and 2 up to at least 2 Hz. Possible

peaks may be discerned at frequencies in the band 15-22 mHz. Even though amplitudes of these peaks seem too high, their frequencies approximate the theoretical main peak frequency of the H/V of a model reflecting average crustal properties beneath the array (Model 2 in Table 1), which appears at 16.6 mHz for FW-H/V and at 17.6 mHz for SW-H/V, slightly below the SH resonance at 19.3 mHz. Unfortunately, these peaks lay around the limit of the sensitivity of the sensors used and this fact implies that decreasing trends below the peak frequency might be an instrumental effect [*Strollo et al*., 2008]. Anomalously high H/V ratios below 0.1 Hz or 0.2 Hz and instability have been associated to action of the gravitational acceleration on the horizontal records due to possible ground tilting generated either by near loads [*Forbriger*, 2007; *Wielandt and Forbriger*, 1999] or by atmospheric pressure variations and wind. These effects can be minimized by using borehole sensors [*Ziolkowski*, 1973; *De Angelis and Bodin*, 2012].

At higher frequencies, experimental curves seem to converge to a common constant level inside a rather broad band from about 0.15 Hz to some frequency between 0.6 Hz and about 2 Hz. H/V ratios for stations PIAL, PGAL and ZUAL result especially stable up to about 0.6Hz while stations UNAL and USAL present some decreasing trend. These ratios have been shown in Fig. 8a-e in the band 0.1 Hz to 2 Hz. The average H/V levels in the frequency band 0.15-0.6 Hz and their standard deviations were 1.17±0.04 for PIAL, 1.28 ± 0.06 for PGAL, 1.28 ± 0.13 for UNAL, 1.22 ± 0.14 for USAL and 1.26 ± 0.08 for ZUAL. If the H/V ratios of these stations are considered as a single dataset, a global value of 1.24 ± 0.11 results for that band, which lays in the narrow interval between the theoretical high-frequency limits for SW (1.13) and for FW (1.33) obtained by assuming Model 2 (Table 1) as representative of the site. This assumption is strictly connected with the consideration of the frequency band 0.15 - 0.6 Hz as representative of the high-frequency limit for the H/V curve, because it is

reasonable to link the significant increasing in some of these curves above 0.6 Hz with very local (i.e., shallow) effects, that could be separated from our discussion. In fact, the reasonable performance of this rough crustal model seems to highlight the absence of comparable impedance contrasts from the Moho up to about 1400 m at least. This minimum depth can be estimated as the penetration of Rayleigh waves at about 0.6 Hz, taking into account some local dispersion curves. In assuming Model 2 structure, it has been checked that the wavefield in the band 0.1 – 2 Hz consists of a large enough number modes, so that the theoretical HVSRs do not present significant differences from their high-frequency limits (derived from assumption of coexistence of multiple modes).

We might reasonably conclude that H/V ratios in this frequency range are compatible with a sort of imperfect diffuse wavefield, probably with a trend to exceed the theoretical share of BW as frequency increases. Nevertheless, uncertainties related with effects of local scale layering, or 2D/3D structures prevent us from stating definitive conclusions and from properly explaining the differences among ratios of different stations. Although Model 2 seems to be suitable to explain H/V ratios, which depend mainly on velocity contrasts and Poisson's coefficients, it could be ineffective for explanation of measurements sensitive to absolute velocities.

Though this article is mainly devoted to their high-frequency behavior, we have checked that H/V ratios at several good-quality seismic stations bear significant resemblance to the curves predicted by simple crustal models in broader bands of frequency. Figure 9 shows results for the Global Seismic Network (GSN) stations ANTO, MAJO, NWAO and TATO in the band from 5 to 45 mHz using four months of continuous record. These stations consist of STS-1, KS-36000 or KS-54000 seismometers, with low enough nominal selfnoise power in the

mentioned band and installed in boreholes or tunnels to minimize perturbations by surface sources described above. The spectral ratios at MAJO, NWAO and ANTO (Fig. 9a), at which the crustal thicknesses estimated by *Reguzzoni and Sampietro* [2012] range between 34 and 39 km, are comparable with calculations from the reference model of continental crust (Model 1 in Table 1, Fig 6c). The increasing trend of the H/V ratio at MAJO site as frequency decreases below 20 mHz is probably due to its shallower installation. This hypothesis is reinforced e.g., by comparison between H/V curves of a borehole and a surface sensor at site NWAO, showing a considerable increasing in low frequencies for the latter one. The main peak for station TATO (in Taipei, Taiwan) seems to be shifted toward higher frequencies suggesting a smaller crustal thickness. In fact, that curve (Fig 9b) compares better to the result of an ad-hoc model reproducing the estimated Moho depth in that area, of about 24 km (Model 3 in Table 1).

5. HIGH-FREQUENCY TREND OF THE AKI'S SPAC COEFFICIENTS

The calculations performed in Section 3 can be also applied to the study of the Aki's vertical (ρ_V), radial (ρ_{rad}) and tangential (ρ_{tg}) spatial autocorrelation (SPAC) coefficients [*Aki*, 1957] at high frequencies for the considered type of structure. As shown below, when a large number of modes coexists, fundamental Rayleigh waves are the only surface waves effectively observed from variations in both ρ_V and ρ_{rad} vs. frequency. Effects of higher Rayleigh-wave modes on ρ_V as well as effects of higher Rayleigh modes and Love waves on ρ_{rad} are limited to a decrease in amplitude by a constant (independent of *f*) factor, preserving the $\propto f^{-1/2}$ decaying trend in amplitude. Coefficient ρ_{tg} presents a more complicated behavior. For small enough interstation distances fulfilling $r/d \le 2\beta_1(\beta_2^2 - \beta_1^2)^{-1/2}$, the tangential cross-correlation would be dominated by low-order

Love modes which build up an oscillatory term of the Green's function with constant amplitude as $f \to \infty$ ($r \neq 0$), in contrast with the $\propto f^{1/2}$ behavior of its vertical and radial counterparts. Consequently, ρ_{tg} decays as f^{-1}, slower than the expected behavior for a single Love-wave mode but faster than ρ_V and ρ_{rad}.

In the context of diffuse wavefields, the Aki's spatial autocorrelation coefficients can be expressed in terms of Green's functions as follows [*Yokoi and Margaryan*, 2008]:

$$\rho_V(\omega, r, \theta) \equiv \frac{1}{P_V} \mathrm{Re}\left\langle u_z(r, \theta; \omega) u_z^*(0; \omega) \right\rangle = \mathrm{Im}\left[G_{zz}(r, \theta; 0; \omega)\right] / \mathrm{Im}\left[G_{zz}(0; 0; \omega)\right], \quad (19)$$

$$\rho_{rad}(\omega, r, \theta) \equiv \frac{1}{P_X} \mathrm{Re}\left\langle u_r(r, \theta; \omega) u_r^*(0, \theta; \omega) \right\rangle = \mathrm{Im}\left[G_{rr}(r, \theta; 0, \theta; \omega)\right] / \mathrm{Im}\left[G_{rr}(0, \theta; 0, \theta; \omega)\right], \quad (20)$$

$$\rho_{tg}(\omega, r, \theta) \equiv \frac{1}{P_X} \mathrm{Re}\left\langle u_\theta(r, \theta; \omega) u_\theta^*(0; \theta; \omega) \right\rangle = \mathrm{Im}\left[G_{\theta\theta}(r, \theta; 0, \theta; \omega)\right] / \mathrm{Im}\left[G_{\theta\theta}(0, \theta; 0, \theta; \omega)\right], \quad (21)$$

where P_X stands for $P_H / 2$ and cylindrical coordinates have been used assuming $z = 0$. Any dependence of the coherences on the azimuth of the pair, θ, disappears for a horizontally layered medium under homogenous illumination. Thus, Eqs. (4-6) and (8-10) can be inserted in (19-21).

Provisionally accepting the hypothesis of predominance of surface waves (a usual assumption in SPAC context), the mentioned Green's functions can be replaced by the contributions of poles to the integrals over *k* [*Harkrider*, 1964], leading to simpler high-frequency asymptotic

forms for ρ_V^{SW}, ρ_{rad}^{SW} and ρ_{tg}^{SW}:

$$\rho_V^{SW} \sim \frac{a_{R0}^V J_0\left[k_{R0}(f)r\right] + \delta^V}{a_{R0}^V + a_{Rhigh}^V}, \tag{22}$$

$$\rho_{rad}^{SW} \sim \frac{a_{R0}^H \left[J_0(k_{R0}r) - J_2(k_{R0}r)\right] + \delta_{R1}^- + \delta_L^+}{a_L + a_{R0}^H + a_{Rhigh}^H}, \tag{23}$$

$$\rho_{tg}^{SW} \sim \frac{\delta_{R0}^+ + \delta_L^-}{a_L + a_{R0}^H + a_{Rhigh}^H}. \tag{24}$$

In these equations, quantities δ^V and δ_{R1}^- gathers all terms of $\mathrm{Im}\left[G_{33}(r,0,0;0;\omega)\right]/f$ and $\mathrm{Im}\left[G_{11}(r,0,0;0;\omega)\right]/f$, respectively, corresponding to higher Rayleigh modes. Quantities δ_{R0}^+, δ_L^+ and δ_L^- are similarly defined, but they also include the corresponding Rayleigh or Love fundamental modes. Taking into account the dependences on *r* shown in equations (4-6) and the high-frequency properties of A_{Lm} and A_{Rm} described in Sections 3.2.1 and 3.2.2, the behavior of these expressions at high frequencies would be:

$$\delta^V \sim \frac{1}{f} \sum_{m=1}^{n(f)} A_{R\infty}[k_{Rm}(f)/m]\, J_0[k_{Rm}(f)\, r], \tag{25}$$

$$\delta_{Rm_0}^{\pm} \sim \frac{1}{f} \sum_{m=m_0}^{n(f)} A_{R\infty}[k_{Rm}(f)/m]\, \chi_\infty^2[k_{Rm}(f)/m] \{J_0[k_{Rm}(f)\, r] \pm J_2[k_{Rm}(f)\, r]\}, \tag{26}$$

$$\delta_L^{\pm} \sim \frac{1}{f}\sum_{m=0}^{n(f)} A_L(\infty)\{J_0[k_{Lm}(f)r] \pm J_2[k_{Lm}(f)r]\}. \quad (27)$$

Except for δ_L^- in (24), it is shown in Appendix C that these contributions become negligible at high frequencies in comparison with the other terms in the numerators of (22), (23) and (24). Therefore, both ρ_V^{SW} and ρ_{rad}^{SW} become dominated by the fundamental Rayleigh mode as frequency increases, provided that $r > 0$. Roughly speaking, the oscillatory behavior of the Bessel's functions prevents the constructive summation of higher Rayleigh-mode powers required to keep a stable joint share at high frequencies (contrary to the $r = 0$ case, Fig. 4, where the linear trend of the fundamental-mode medium response was effectively achieved by the rest of Rayleigh modes). In the tangential-component case, Rayleigh wave contributions to ρ_{tg}^{SW}, i.e. δ_{R0}^+, decay rapidly as frequency grows, following the $f^{-3/2}$ behavior of $J_0[k_{Rm}(f)r] + J_2[k_{Rm}(f)r]$, while the cumulative effect of Love modes (i. e. δ_L^-) does build up one or several dominant $\propto f^{-1}$ contributions to ρ_{tg}^{SW} ($\propto f^0$ in terms of $\mathrm{Im}[G_{22}(r,0,0;0;\omega)]/f$).

After removing the negligible contributions to ρ_V^{SW}, ρ_{rad}^{SW} and ρ_{tg}^{SW} and introducing the definitions $\eta_V^{SW} = a_{R0}^V (a_{R0}^V + a_{R\,high}^V)^{-1}$, $\eta_{rad}^{SW} = a_{R0}^H \left(a_L + a_{R0}^H + a_{R\,high}^H\right)^{-1}$ and $\eta_{tg}^{SW} = 4\rho_1^{-1}\beta_1^{-3}\left(a_L + a_{R0}^H + a_{R\,high}^H\right)^{-1}$, equations (22), (23) and (24) yield:

$$\rho_V^{SW} \sim \eta_V^{SW} J_0(k_{R0}r), \quad (28)$$

$$\rho_{rad}^{SW} \sim \eta_{rad}^{SW}[J_0(k_{R0}r) - J_2(k_{R0}r)], \quad (29)$$

$$\rho_{tg}^{SW} \sim \eta_{tg}^{SW} j_0(k_{\beta_1} r) \ , \ r \le 2d\beta_1 / \sqrt{\beta_2^2 - \beta_1^2} \ . \tag{30}$$

The above expression for ρ_{tg}^{SW} corresponds to the simplest case of $r \le 2d\beta_1 / \sqrt{\beta_2^2 - \beta_1^2}$, for which δ_L^- (and ρ_{tg}^{SW}) is dominated by waves of horizontal velocity β_1 generated by interference of the low-order modes. Note that the zero-order spherical Bessel function $j_0(\cdot)$ in Eq. (30) is also the form of the SH contribution to the cross correlation of horizontal components in a 3D full space, in the sense described by *Sánchez-Sesma and Campillo* [2006, equation 35]. This result, as well as the analysis of ρ_{tg}^{SW} for arbitrary *r*, is discussed in Appendix C. It is worth to note that the approximations expressed in Eqs. (28, 29, 30) hold for large values of the Bessel functions arguments and, in particular, $r \neq 0$ is required. The fact that their value for interstation distances tending to zero is different from one generates no contradiction.

For Model 1, effects of higher modes at high frequencies represent an 18% decrement in amplitude for ρ_V^{SW} ($\eta_V^{SW} = 0.818$) and a 71% amplitude reduction for ρ_{rad}^{SW} ($\eta_{rad}^{SW} = 0.29$) over the predicted values for a hypothetical wavefield consisting of fundamental-mode Rayleigh waves. Finally, η_{tg}^{SW} is 1.99 for this model. Synthetic examples of application of these results to that simple crustal model, accounting only for surface waves, have been displayed in Figs. 10 and 11 for interstation distances of 35 km and 110 km, respectively. As shown, the predicted asymptotic behaviors (dashed black lines) match well the theoretical Green's functions and SPAC coefficients (thick gray lines) at high frequencies. Since this is a frequently assumed hypothesis in experimental studies, calculations restricted to fundamental

Rayleigh- and Love-wave modes (simultaneously acting) have been shown for reference (solid black lines). Coefficient ρ_V^{SW} is well reproduced by the fundamental (Rayleigh) mode except for the very slight variation in amplitude. On the contrary, the amplitudes of ρ_{rad}^{SW} are substantially overestimated by using fundamental modes, since Love wave contributions to the normalization factor P_X are almost completely ruled out if higher modes are disregarded. Oscillations in ρ_{tg}^{SW} can be precisely explained neither in amplitude nor in phase by using fundamental modes. Nevertheless, the resulting misfit in ρ_{tg}^{SW} is moderate, due to partial cancellation of the effects of suppressing higher Love modes in both the numerator and denominator of (21). Note that r/d is greater than $2\beta_1(\beta_2^2-\beta_1^2)^{-1/2}$ in Fig. 11, making possible the existence of several (two) superimposed contributions to ρ_{tg}^{SW} with significant power, as shown in Fig.11f (see Appendix C for details).

Effects of body waves can be partly introduced in equations (28), (29) and (30) replacing terms $\left(a_{R0}^V + a_{R\,high}^V\right)/2$ and $\left(a_L + a_{R0}^H + a_{R\,high}^H\right)/2$ in the denominators of η_V^{SW}, η_{rad}^{SW}, and η_{tg}^{SW} with their FW counterparts, which can be computed considering a halfspace with upper layer properties as $-\mathrm{Im}[G_{33}^{HS}(0;0;\omega)]/f$ and $-2\,\mathrm{Im}[G_{11}^{HS}(0;0;\omega)]/f$, respectively (see Eqs. 8-10 and red lines in Figs. 2a,b apart from the $\rho_1\beta_1^3$ factor). This simple procedure is suitable provided that terms in the Green's function involving body waves represent negligible contributions to $\mathrm{Im}[G_{jj}(r,0,0;0;\omega)]$ at high frequencies for $r\neq 0$ (and consequently to the cross-correlation) in comparison with those of surface-waves. Several theoretical works point to the adequateness of this assumption [e.g., *Tamura*, 1996]. In this case, consideration of body waves simply implies additional decreasing in the amplitude of the SPAC coefficients from their SW counterparts, due to the incremented estimations of the power spectral

densities used for normalization. Specifically, for Model 1, quantity η_V drops from 0.82 to 0.67, η_{rad} varies from 0.29 to 0.18, and η_{tg} changes from 1.99 to 1.22 (Fig. 12). Figs. 13c-e and 14c-e show simulated FW SPAC coefficients (thick gray lines) together with the FW asymptotic forms derived in this way (dashed black lines). Due to the moderate relative power of body waves (39% of P_H and 17.6% of P_V, at high frequencies), the decreases in ρ_V, ρ_{tg}, and ρ_{rad} amplitudes due to body waves remain moderate, being accurately modeled by using FW power densities for normalizing SW cross correlations.

Assuming that this type of multiple-mode propagation effects at high frequencies may appear for more general profiles, it is suggested to use full wavefield modeling as a general practice for interpretation of coherences in inversions of velocity or attenuation structures. Attending to the results for a simple model, this fact would be important when dealing with horizontal components and essential for using tangential coherences. Alternatively, any processing scheme insensitive to a constant scaling factor would be suitable for interpretation of vertical SPAC coefficients in terms of fundamental Rayleigh mode in broad frequency bands (e.g., by using data of zero crossings or positions of maxima and minima instead of using amplitudes). Bands wherein two or only a few modes coexist are unsuitable for using these simple schemes.

6. CONCLUSIONS

Explicit expressions for the horizontal- and vertical-component power spectra (P_H, P_V) at the surface of a horizontally layered structure due to a diffuse wavefield have been derived on the basis of Harkrider`s formulation of the Green's function. These expressions, based on classic contour integration in the complex-wavenumber plane allow separate calculation of *P-SV*,

SH, Rayleigh and Love wave components. Harkrider`s notation is also used for surface waves terms. Their application to the particular case of a simple waveguide consisting of a plane layer overlying a stiffer halfspace provides new insight into the roles of different propagation modes at low- and high-frequencies, extending previous results obtained by *Margerin et al.* [2009].

The results for low frequencies rely on the semi-infinite medium formulation derived by *Weaver* [1985], evaluated at the halfspace properties. Even though the total P_H and P_V powers at high frequencies also follow Weaver's expressions for the upper layer properties (ν_1), halfspace velocity is involved in the partitions between different types of waves. P_H and P_V at high-frequencies have been broken down into the contributions of the different types of waves, for which analytical formulae or expressions allowing straightforward computation have been given. To the best of the authors' knowledge, the derivations of total power of higher Rayleigh modes are original.

For a simple model of the crust and upper mantle (Model 1), the high-frequency surface wavefield in the horizontal-component should be made up of 68.3% of Love waves, without preference among the active modes, 29.1% of fundamental-mode Rayleigh waves and 2.6% for higher-mode Rayleigh waves. The vertical surface wavefield is dominated by the fundamental Rayleigh mode (81.8%). Body waves carry the 39.0% and the 17.6% of the horizontal and vertical powers, respectively.

Under diffuse field approximation, the theoretical high-frequency limit of the SW-H/V spectral ratio for this crustal model is expected to be 1.14. Since this value is close to the FW result, 1.33, empirical selection of the best of these models is difficult in this manner. The average result of an experiment performed with five stations deployed in the western

Pyrenean edge was 1.24 ± 0.11. The FW-H/V limit is independent of the halfspace properties, whereas the SW-H/V limit does depend on the S-wave velocity contrast, due to the sensitivity of the contributions of higher Rayleigh modes to this ratio. Limits of both models are obviously insensitive to the layer thickness.

Even though arguments based on the H/V ratio can be regarded only as an indirect test of the diffusive wavefield hypothesis, our experimental results support its applicability for ambient noise in the studied range of frequencies. Hypotheses of diffuse field have been already checked in careful experiments with seismic coda in higher frequency bands. E.g., *Hennino et al.* [2001] found excellent accord between energy ratios involving kinetic, compressional and shear energy densities and predictions for a Poisson's halfspace between 1 and 3 Hz, while some overestimation of the Rayleigh-wave content was considered to precisely explain the experimental H^2/V^2 ratio. Using surface and subsurface records, *Nakahara and Margerin* [2011] have confirmed that experimental H/V ratios for the S-wave coda are better fitted by a diffuse wavefield consisting of pure body waves at frequencies above 5 Hz. Nevertheless, effects of surface layering are not negligible at those frequencies even for rock sites, complicating the accurate modeling. Though additional work is needed, our results also point to the sensitivity of ambient noise H/V shape to crustal resonances from frequencies around the tens of mHz, provided that low-noise and well installed borehole instruments are used.

Finally, effects of the mixture of multiple surface-wave modes as well as body waves on the Aki's SPAC coefficients have been analyzed at high frequencies. Our analytical derivations and numerical tests for a simple model demonstrate that vertical and radial coherences correspond with Rayleigh fundamental-mode curves decremented in amplitude by predictable frequency-independent factors. This decrement is due to the share of Love waves (in the case

of ρ_{rad}) and higher Rayleigh modes (for both ρ_V and ρ_{rad}) on the power spectra used for normalization. Effects on ρ_{rad} may be particularly intense, due to the major role usually played by Love waves in P_H. On the other hand, effects of higher modes on ρ_{tg} are described, for small enough interstation distances, by a variation in the decay rate of its envelope with frequency, as well as a phase change in the oscillations of $\rho_{tg}(f)$, in comparison with calculations based on fundamental modes. Effects of body waves on SPAC coefficients at high frequencies have been successfully approximated by using FW power densities P_X, P_V (or autocorrelations) as normalization factors and keeping cross correlations restricted to SW. Comparison between theoretical H/V ratio and coherences derived from the DFA and parallel results based on random distributions of surface sources [e.g., *García-Jerez et al.*, 2012] should be discussed in detail in future work.

Analysis of anelastic attenuation from ambient noise coherences is still an insufficiently explored field. Papers by *Prieto et al.* [2009], *Tsai* [2011], *Lin et al.* [2011] and *Weaver* [2013] can be mentioned between the pioneering works in this area. In particular, Weaver proposed to model spatially varying attenuation using the radiative transfer equation. It is expected that the new results found in this work will be helpful for clarification of the oscillatory behavior of coherences, avoiding misinterpretation of effects of wavefield complexity in terms of anelastic attenuation.

APPENDIX A

Derivation of equations (16) and (17) is addressed herein. Firstly, it can be shown that functions A_{Rm} and χ_m tend to certain function of (k_{Rm}/m) as m increases, say $A_{R\infty}[k_{Rm}/m]$ and $\chi_\infty[k_{Rm}/m]$ (as shown in Fig. 5).

The limit function $A_{R\infty}[\cdot]$ does not depend on m or f. Although the expression of $A_{R\infty}$ is somewhat complicated, it can be obtained by using suitable software for symbolic computation, such as Mathematica®. For example, we have started from the original Harkrider's expression of the medium response [*Harkrider*, 1964], evaluating $\partial[NK-LM]/\partial k$ analytically as a function of k and c. Afterwards, it is particularized for the m-th mode and $A_{Rm}=-i[GN-LH][\partial(NK-LM)/\partial k]^{-1}$ is rewritten as a function of k_{Rm}/m, $1/m$ and the phase velocity of the m-th mode c_{Rm}. Then, c_{Rm} is expressed in terms of (k_{Rm}/m) by means of approximate expression of the m-th mode dispersion curve (Appendix B) and terms with $O(1/m)$ behavior are disregarded.

The expression of $\chi_{\infty}[\cdot]$ can be also derived taking the limit $m\to\infty$ in the general Haskell's expression of iK/L (ellipticity) [*Haskell*, 1953]. The halfspace formula (11) arises provided that it is evaluated at α_1, β_1 and the (frequency-dependent) phase velocity $c_{Rm}(f)$, that is:

$$\chi_m(f)\to\chi_{HS}[\alpha_1,\beta_1,c_{Rm}(f)]=\frac{2-c_{Rm}^2/\beta_1^2}{2\sqrt{1-c_{Rm}^2/\alpha_1^2}}\ . \tag{A1}$$

Considering that $c_{Rm}(f)$ tends to a function of k_{Rm}/m as m tends to infinity (see Eq. B1), the ellipticity of a very high mode can be alternatively written as:

$$\chi_m(f)\to\chi_{\infty}[k_{Rm}/m]=\chi_{HS}[\alpha_1,\beta_1,\beta_1\sqrt{\frac{\pi^2}{d^2(k_{Rm}/m)^2}+1}]. \tag{A2}$$

Since the medium response A_{Rm} of any particular mode *m*, different from the fundamental one, shows an f^{-2} decaying behavior at high enough frequencies while the total sum $\sum_{m=1}^{n} A_{Rm}$ grows proportionally to *f* (Fig. 4), the contribution of a finite subset of higher modes to the sum becomes negligible as frequency grows. Thus, the total contribution of higher modes to the high frequency trend of P_V can be calculated disregarding the effects of the finite number low-order modes for which A_{Rm} significantly differs from $A_{R\infty}$, i. e. by using $A_{R\infty}(k_m / m)$ function for all the modes. For simplicity, let *f* grow to infinity with discrete increments through the successive Rayleigh mode cutoff frequencies f_{Rn}^{c}, *n* = 1, 2, … Thus, replacing $A_{Rm}(f_{Rn}^{c})$ with $A_{R\infty}[k_{Rm}(f_{Rn}^{c})/m]$ for any *m* and *n* we obtain:

$$a_{R\,high}^{V} = \lim_{n->\infty} \frac{1}{f_{Rn}^{c}} \sum_{m=1}^{n-1} A_{R\infty}[k_{Rm}(f_{Rn}^{c})/m] \ . \tag{A3}$$

In principle, detailed knowledge of the dispersion curves in terms of $k_{Rm}(f)$ (including their respective cutoff frequencies) should be required for evaluation of (A3). Nevertheless, we realize from the previous discussions that precision is needed for *m* larger than an arbitrary threshold only. Therefore, we are allowed to make use of the following expressions (see Appendix B):

$$f_{Rn}^{c} = \frac{n}{2d} \frac{\beta_2}{\sqrt{\beta_2^2 / \beta_1^2 - 1}} + O(n^0) \ , \tag{A4}$$

$$\frac{k_{Rm}(f_{Rn}^{c})}{m} = \frac{\pi}{d} \sqrt{\frac{\beta_2^2}{(\beta_2^2 - \beta_1^2)(m/n)^2} - 1} + O(1/m) + O(1/n) \ , \tag{A5}$$

which can be evaluated without computing any particular dispersion curve and, consequently, avoid the necessity of numerical calculation of Rayleigh roots. Thus, replacing these truncated series in (A3) we finally find:

$$a^{V}_{R\,high} = \frac{2d\sqrt{\beta_2^2/\beta_1^2-1}}{\beta_2}\lim_{n\to\infty}\frac{1}{n}\sum_{m=1}^{n-1} A_{R\infty}[\frac{\pi}{d}\sqrt{\frac{\beta_2^2}{(\beta_2^2\text{-}\beta_1^2)(m/n)^2}-1}] =$$

$$\frac{2d\sqrt{\beta_2^2/\beta_1^2-1}}{\beta_2}\int_0^1 d\xi A_{R\infty}[\frac{\pi}{d}\sqrt{\frac{\beta_2^2}{(\beta_2^2\text{-}\beta_1^2)\xi^2}-1}]\,, \qquad \text{(A6)}$$

where the variable ξ represents m/n.

The calculation of the contribution of higher Rayleigh modes to P_H, can be carried out by following a similar procedure:

$$a^{H}_{R\,high} = \frac{2d\sqrt{\beta_2^2/\beta_1^2-1}}{\beta_2}\lim_{n->\infty}\frac{1}{n}\sum_{m=1}^{n-1}\chi^2_{\infty}[\frac{\pi}{d}\sqrt{\frac{\beta_2^2}{(\beta_2^2\text{-}\beta_1^2)(m/n)^2}-1}]\,A_{R\infty}[\frac{\pi}{d}\sqrt{\frac{\beta_2^2}{(\beta_2^2\text{-}\beta_1^2)(m/n)^2}-1}]$$

$$= \frac{2d\sqrt{\beta_2^2/\beta_1^2-1}}{\beta_2}\int_0^1 d\xi\chi^2_{\infty}[\frac{\pi}{d}\sqrt{\frac{\beta_2^2}{(\beta_2^2\text{-}\beta_1^2)\xi^2}-1}]A_{R\infty}[\frac{\pi}{d}\sqrt{\frac{\beta_2^2}{(\beta_2^2\text{-}\beta_1^2)\xi^2}-1}]\,. \qquad \text{(A7)}$$

APPENDIX B

We herein derive the lowest order term of suitable power series expansions for i) the *n*-th Rayleigh mode cutoff frequency f^c_{Rn} and ii) the *m*-th mode normalized wavenumber k_{Rm}/m evaluated at f^c_{Rn}. A model consisting of a single layer overlying a halfspace for which $\beta_1 < \alpha_2$ is assumed. These functions are expanded on variables *n* and *m*.

It can be demonstrated from the equation defining the Rayleigh wave velocities in this model [e.g., *Ben-Menahem and Singh*, 2000, equation 3.119] that higher-mode dispersion curves, expressed as $c_{Rm}(k_{Rm})$, fulfill the relation:

$$\frac{k_{Rm}}{m} = \frac{\pi}{d\sqrt{c_{Rm}^2/\beta_1^2 - 1}} + O(1/m) \quad , \; \beta_1 < c_{Rm} < \beta_2 \, . \tag{B1}$$

Thus, the expected formula for f_{Rn}^c can be simply obtained by using (B1) for the *n*-th higher mode and taking its value at its cutoff frequency, (at which, $c_{Rn} = \beta_2$):

$$f_{Rn}^c = \frac{\beta_2 k_{Rn}^c}{2\pi} = \frac{n}{2d} \frac{\beta_2}{\sqrt{\beta_2^2/\beta_1^2 - 1}} + O(n^0) \, , \tag{B2}$$

i. e. the rate of generation of Rayleigh modes as frequency increases is same as for Love waves. Provided that $m < n$, the cutoff circular frequency of the *n*-th mode, $2\pi f_{Rn}^c$, may also be written in terms of the *m*-th mode dispersion curve as $k_{Rm}(f_{Rn}^c)$ $c_{Rm}(f_{Rn}^c)$. Equaling these alternative expression of $2\pi f_{Rn}^c$ and using (B1) also for mode *m*, we obtain

$$\beta_2 \frac{n\pi}{d\sqrt{\beta_2^2/\beta_1^2 - 1}} + O(n^0) = c_{Rm} \frac{m\pi}{d\sqrt{c_{Rm}^2/\beta_1^2 - 1}} + O(m^0) \, . \tag{B3}$$

Explicit indications of evaluation at f_{Rn}^c have been provisionally removed in the sake of simplicity. Since we are interested in cases of large values of *n* and *m* but arbitrary *m*/*n* ratio

(apart from the constraint m/n <1), equation (B3) should be better rewritten as:

$$\beta_2 \frac{\pi}{d\sqrt{\beta_2^2/\beta_1^2-1}} + O(1/n) = c_{Rm}\left(\frac{m}{n}\right)\frac{\pi}{d\sqrt{c_{Rm}^2/\beta_1^2-1}} + O(1/n)\,. \tag{B4}$$

Working out c_{Rm} from (B4) we obtain

$$c_{Rm} = \frac{\beta_1\beta_2}{\sqrt{\beta_2^2+(\beta_1^2-\beta_2^2)(m/n)^2}} + O(1/n)\,, \tag{B5}$$

which can be finally replaced in the right hand side equation of (B1), leading to

$$\frac{k_{Rm}(f_{Rn}^c)}{m} = \frac{\pi}{d}\sqrt{\frac{\beta_2^2}{(\beta_2^2\text{-}\beta_1^2)(m/n)^2}-1} + O(1/m) + O(1/n)\,, \tag{B6}$$

where the evaluation at f_{Rn}^c has been highlighted again.

APPENDIX C

The relative weights at high frequencies of the terms δ^V, δ_{R0}^+, δ_{R1}^- and $\delta_L^\pm$ in equations (22), (23) and (24) are investigated in this appendix. The behavior of δ_{R0}^+ can be immediately derived considering that it is the sum of δ_{R1}^+ plus the contribution of the fundamental Rayleigh mode (with amplitude decaying $\propto f^{-3/2}$ in this case). In order to find out their asymptotic behaviors we start from equations (25), (26) and (27) replacing the Bessel functions with the respective large-argument approximations. For large enough values of *f*,

these quantities can be generically approximated as:

$$\delta^{s}_{m_0} \sim -\frac{2s}{\pi^{1/2} f} \sum_{m=m_0}^{n} A[k_m(f)/m] \left[\frac{2}{k_m(f) r}\right]^{1+s/2} \cos\left[k_m(f) r + s\frac{\pi}{4}\right], \qquad \text{(C1)}$$

where s takes values ± 1, A stands for $A_{R\infty}[\cdot]/2$, $A_{R\infty}[\cdot]\,\chi^2_{\infty}[\cdot]$ or $A_{L\infty}[\cdot]$ and $k_m(f)$ represents either $k_{Rm}(f)$ or $k_{Lm}(f)$. δ^{V} follows the case $s = -1$ with starting mode $m_0 = 1$ whereas $m_0 = 0$ is used for $\delta^{\pm}_{L}$. We now introduce the normalized frequency $n_h = f / f_1^c$, with IntegerPart[n_h] coinciding with the number of existing higher modes at *f*. Since the dispersion curve fulfill a generic eigenvalues equation $F(m, k, f) = 0$, we can define a normalized wavenumber $\tilde{k}(\xi, n_h)$ as the real positive solution of $G(\xi, \tilde{k}, n_h) = 0$, with $G(\xi, \tilde{k}, n_h) = F(\xi\, n_h, n_h\, \tilde{k}, n_h\, f_1^c)$, so that the wavenumber of the *m*-th mode at frequency *f* (i.e. $k_m(f)$) is $n_h\, \tilde{k}(m/n_h, n_h)$. Quantity ξ is allowed to take real values between 0 and 1. Function $\tilde{k}(\xi, n_h)$ converges to a simple function of ξ as n_h tends to infinity. The sum in (C1) can be rewritten in terms of integrals by using Dirac's deltas:

$$\begin{aligned}
\delta^{s}_{m_0} &\sim -\frac{2s}{\pi^{1/2} n_h f_1^c} \sum_{m=0}^{n} \int_{-\infty}^{+\infty} A(\xi) \left[\frac{2}{n_h \tilde{k}(\xi, n_h) r}\right]^{1+s/2} \cos\left[n_h \tilde{k}(\xi, n_h) r + s\frac{\pi}{4}\right] \delta(\xi - \frac{m}{n_h}) d\xi \\
&= -\frac{2s}{\pi^{1/2} n_h f_1^c} \int_{-\varepsilon}^{1} A(\xi) \left[\frac{2}{n_h \tilde{k}(\xi, n_h) r}\right]^{1+s/2} \cos\left[n_h \tilde{k}(\xi, n_h) r + s\frac{\pi}{4}\right] \sum_{m=-\infty}^{+\infty} \delta(\xi - \frac{m}{n_h}) d\xi \\
&= -\frac{2s}{\pi^{1/2} n_h f_1^c} \int_{-\varepsilon}^{1} A(\xi) \left[\frac{2}{n_h \tilde{k}(\xi, n_h) r}\right]^{1+s/2} \cos\left[n_h \tilde{k}(\xi, n_h) r + s\frac{\pi}{4}\right] \Delta_{1/n_h}(\xi) d\xi \qquad \text{(C2)}
\end{aligned}$$

where $\Delta_T(\cdot)$ represents the Dirac's comb (i. e. a periodic delta function) with generic period T and ε stands for a small positive quantity (smaller than $1/n_h$) assuring that the contribution for $m = 0$ is summed. Extension of the sum over index m to negative integers and to integers greater than n has no consequence since the corresponding values of m/n_h lay outside the integration interval. At this point, we can take advantage of a suitable representation of $\Delta_T(x)$ as $\Delta_T(x) = T^{-1}\sum_{j=-\infty}^{\infty} e^{i2\pi jx/T} = T^{-1}\{1 + 2\sum_{j=1}^{\infty}\cos[2\pi jT^{-1}x]\}$, to rewrite the previous expression as:

$$\delta^s_{m_0} \sim -\frac{2s}{\pi^{1/2} f_1^c}\int_{-\varepsilon}^{1} A(\xi)\left[\frac{2}{n_h \widetilde{k}(\xi, n_h) r}\right]^{1+s/2} \cos\left[n_h \widetilde{k}(\xi, n_h) r + s\frac{\pi}{4}\right] \times$$

$$\left\{1 + 2\sum_{j=1}^{\infty}\cos[2\pi n_h j\xi]\right\} d\xi = -\frac{2s}{\pi^{1/2} f_1^c n_h^{1+s/2}}\int_{-\varepsilon}^{1} A(\xi)\left[\frac{2}{\widetilde{k}(\xi, n_h) r}\right]^{1+s/2} \times \cos\left[n_h \widetilde{k}(\xi, n_h) r + s\frac{\pi}{4}\right] d\xi$$

$$-\frac{2s}{\pi^{1/2} f_1^c n_h^{1+s/2}}\sum_{j=1}^{\infty}\int_{-\varepsilon}^{1} A(\xi)\left[\frac{2}{\widetilde{k}(\xi, n_h) r}\right]^{1+s/2} \times$$

$$\left\{\cos\left[n_h \widetilde{k}(\xi, n_h) r + 2\pi n_h j\xi + s\frac{\pi}{4}\right] + \cos\left[n_h \widetilde{k}(\xi, n_h) r - 2\pi n_h j\xi + s\frac{\pi}{4}\right]\right\} d\xi \,. \qquad \text{(C3)}$$

Finally, integrals in (C3) can be asymptotically approached for high frequencies (i. e., large values of n_h) by means of the stationary phase method [e. g., *Ben-Menahem and Singh*, 2000, pp. 985-986]. For more direct application of this method, cosines may be expressed as real parts of exponentials of imaginary quantities, and functions $\widetilde{k}(\xi, n_h)$ expanded in a power series about $n_h = \infty$, neglecting $O(1/n_h^2)$ terms. It follows that the results of these integrals are $O(n_h^{-1/2})$, though the slower decreasing rate (amplitude $\propto n_h^{-1/2}$) only holds if stationary

phase points exists in the integrand. Taking into account the external factor $n_h^{-1-s/2}$, the slower decrease in amplitude for $\delta_{m_0}^s$ can be $\propto f^{-(3+s)/2}$ and, in particular, any of these quantities will decrease as f^{-1} or faster. In the cases of ρ_V^{SW} and ρ_{rad}^{SW}, the amplitude of the fundamental-mode Rayleigh contribution decreases as slow as $\propto f^{-1/2}$, being therefore the predominant term at high frequencies. On the contrary, the contribution of fundamental-mode Rayleigh waves to ρ_{tg}^{SW} presents a rapid $\propto f^{-3/2}$ decrement in amplitude (due to the dependence on $J_0(k_{R0})+J_2(k_{R0})$), implying that δ_L^- becomes the dominant contribution, with $\propto f^{-1}$ decaying amplitude, provided that stationary phase points exist. The rest of this appendix is devoted to evaluation of δ_L^- so that equation (C3) has to be considered in the case *s*=−*1* and the normalized wavenumber $\tilde{k}(\xi,n_h)=\tilde{k}_L(\xi,n_h)$ can be now precisely defined as the real positive solution of

$$d\sqrt{\left(\frac{2\pi f_{L1}^c}{\beta_1}\right)^2-\tilde{k}_L^2}=\xi\pi+\frac{1}{n_h}\arctan\left(\frac{\mu_2}{\mu_1}\sqrt{\frac{\tilde{k}_L^2-\left(\frac{2\pi f_{L1}^c}{\beta_2}\right)^2}{\left(\frac{2\pi f_{L1}^c}{\beta_1}\right)^2-\tilde{k}_L^2}}\right) \qquad \text{(C4)}$$

[e. g., *Ben-Menahem and Singh*, equation 3.74]. Function $\tilde{k}_L(\xi,n_h)$ is bounded between $\pi d^{-1}\beta_1(\beta_2^2-\beta_1^2)^{-1/2}$ and $\pi d^{-1}\beta_2(\beta_2^2-\beta_1^2)^{-1/2}$. Explicit expressions for $\xi(\tilde{k}_L,n_h)$ and $\tilde{k}_L'(\tilde{k}_L,n_h)=[\partial\tilde{k}_L/\partial\xi]_{\xi(\tilde{k}_L)}$ can be derived from (C4).

Thus, the stationary points, i.e. those values of ξ for which the derivatives of the arguments of any of the cosines listed in (C3) vanish have to be found. Since $\partial\tilde{k}_L(\xi,n_h)/\partial\xi<0$ and *j* is

positive, no stationary point may exist for $\cos[n_h\tilde{k}_L(\xi,n_h)r-2\pi n_h j\xi-\pi/4]$. On the contrary, stationary-phase points may be present in $\cos[n_h\tilde{k}_L(\xi,n_h)r+2\pi n_h j\xi-\pi/4]$ for low enough values of *j*. Since $\tilde{k}_L(\xi,\infty)=\pi d^{-1}[\beta_2^2(\beta_2^2-\beta_1^2)^{-1}-\xi^2]^{1/2}$ (immediate from C4), it is clear that these stationary points tend to $\xi^j=\beta_2\,(\beta_2^2-\beta_1^2)^{-1/2}\,(2^{-2}j^{-2}d^{-2}r^2+1)^{-1/2}$ as n_h tends to infinity, corresponding to with $\tilde{k}_L^j(\infty)\equiv\tilde{k}_L(\xi^j,\infty)=\pi\beta_2 rd^{-1}\,(\beta_2^2-\beta_1^2)^{-1/2}$ $(4d^2j^2+r^2)^{-1/2}$. In this limit case, the condition $\xi^j<1$ implies $j<r(2d\beta_1)^{-1}(\beta_2^2-\beta_1^2)^{1/2}$ and therefore IntegerPart$[r(2d\beta_1)^{-1}(\beta_2^2-\beta_1^2)^{1/2}]$ represents the upper bound for *j* in (C3) for high enough frequencies. Consequently, no solution of this family can be found at short distances fulfilling $r\le 2d\beta_1(\beta_2^2-\beta_1^2)^{-1/2}$. For finite n_h, the values of $\tilde{k}_L^j$ corresponding to stationary phases can be computed as the solutions of $\tilde{k}_L'(\tilde{k}_L,n_h)+2\pi j/r=0$. This task can be efficiently performed by using standard numerical techniques. Alternatively, the solution can be approximated by means of a power series expansion of $\tilde{k}_L$ about the point ($\tilde{k}_L'=-2\pi j/r$, $n_h=\infty$). The constant term is $\tilde{k}_L^j(\infty)$ while the term proportional to n_h^{-1} can be obtained by using the cyclic product rule of partial derivatives: $(\partial\tilde{k}_L/\partial n_h^{-1})_{\tilde{k}_L'}=-(\partial\tilde{k}_L'/\partial n_h^{-1})_{\tilde{k}_L}(\partial\tilde{k}_L'/\partial\tilde{k}_L)^{-1}_{n_h^{-1}}$. At $\tilde{k}_L'=-2\pi j/r$ the series is

$$\tilde{k}_L^j(n_h)=\frac{\pi\beta_2 r}{d\sqrt{(\beta_2^2-\beta_1^2)(4d^2j^2+r^2)}}-\frac{4\beta_1^2\beta_2(\beta_2^2-\beta_1^2)dj^2r\rho_1\rho_2[\beta_2^2r^2-\beta_1^2(4d^2j^2+r^2)]^{-1/2}}{4\beta_1^4d^2j^2\rho_1^2+\beta_2^2[\beta_2^2r^2-\beta_1^2(4d^2j^2+r^2)]\rho_2^2}\left(\frac{1}{n_h}\right)+O\left(\frac{1}{n_h}\right)^2, \quad \text{(C5)}$$

and the corresponding stationary phase point ξ^j, calculated by substitution of (C5) into

$\xi(\widetilde{k}_L, n_h)$ and expansion about $n_h = \infty$, results

$$\xi^j = \frac{2\beta_2 dj}{\sqrt{(\beta_2^2 - \beta_1^2)(4d^2 j^2 + r^2)}} - \frac{1}{\pi}\arctan\left[\frac{\beta_2\rho_2\sqrt{\beta_2^2 r^2 - \beta_1^2(4d^2 j^2 + r^2)}}{2\beta_1^2\rho_1 dj}\right]\left(\frac{1}{n_h}\right) +$$

$$\left[\frac{2dj\beta_1^2\beta_2(\beta_2^2 - \beta_1^2)\rho_1\rho_2 r^2[\beta_2^2 r^2 - \beta_1^2(4d^2 j^2 + r^2)]^{-1/2}}{4\pi\beta_1^4 d^2 j^2\rho_1^2 + \pi\beta_2^4 r^2\rho_2^2 - \pi\beta_1^2\beta_2^2\rho_2^2(4d^2 j^2 + r^2)}\right]\left(\frac{1}{n_h}\right) + O\left(\frac{1}{n_h}\right)^2 . \quad \text{(C6)}$$

The second derivatives $\widetilde{k}_L^{"j}(n_h) = d^2\widetilde{k}_L(\xi^j, n_h)/d\xi^2$ are given by

$$\widetilde{k}_L^{"j}(n_h) = -\pi\frac{\sqrt{\beta_2^2 - \beta_1^2}}{\beta_2 d}(4\frac{d^2}{r^2}j^2 + 1)^{3/2} + O(\frac{1}{n_h}) \ , j \geq 1. \quad \text{(C7)}$$

Note that $\widetilde{k}_L^j(n_h)\left|\widetilde{k}_L^{"j}(n_h)\right| = \pi^2\left(d^{-2} + 4j^2 r^{-2}\right) + O(n_h^{-1})$ tend to positive non-diverging values as n_h tends to infinity. Since $[\widetilde{k}_L^j(n_h)\left|\widetilde{k}_L^{"j}(n_h)\right|]^{-1/2}$ control their amplitudes [*Ben-Menahem and Singh*, 2000, pp. 986], this property guarantees the stability of these oscillatory contributions to (C3) at high frequencies.

Irrespective of the interstation distance, an additional stationary-phase point arise in the argument of $\cos[n_h\widetilde{k}_L(\xi, n_h)r - \pi/4]$ at $\xi^0 = -1/(2n_h)$, with wavenumber

$$\widetilde{k}_L^0 = \frac{\beta_2\pi}{d\sqrt{\beta_2^2 - \beta_1^2}} = \frac{2\pi f_{L1}^c}{\beta_1} = \frac{2\pi f}{\beta_1 n_h} \ , \quad \text{(C8)}$$

i.e. corresponding to waves propagating with velocity β_1 . The second derivative of $\widetilde{k}_L$ at ξ^0 is

$$\widetilde{k}_L^{"0}(n_h) = -\frac{\beta_2^3\sqrt{\beta_2^2-\beta_1^2}\,n_h^2\pi^3\rho_2^2}{d(\beta_1^2\rho_1+n_h\pi\beta_2^2\rho_2)^2} = -\frac{\pi\sqrt{\beta_2^2-\beta_1^2}}{\beta_2 d}+O(\frac{1}{n_h}) \ . \qquad \text{(C9)}$$

As in the previous case, $\widetilde{k}_L^0(n_h)\left|\widetilde{k}_L^{"0}(n_h)\right| = \pi^2/d^2 + O(1/n_h)$ converges as n_h grows, leading to an oscillatory contribution to δ_L^- of stable amplitude. There is still one more stationary-phase point at $\xi = 1$ (waves propagating with velocity β_2). Nevertheless, $d^2\widetilde{k}_L(1,n_h)/d\xi^2$ increases proportionally to n_h^2 as n_h tends to infinity, leading to a contribution of decreasing amplitude for increasing *f* which can be neglected in comparison with the other terms. Therefore, we finally find that δ_L^- behaves as

$$\begin{aligned}\delta_L^- &\sim \frac{2A_L(\infty)}{fr}\sqrt{\frac{1}{\widetilde{k}_L^0\left|\widetilde{k}_L^{"0}\right|}}\sin\left[n_h\widetilde{k}_L^0\, r\right]+\frac{4A_L(\infty)}{fr}\sum_{j=1}^{j_{\max}}\sqrt{\frac{1}{\widetilde{k}_L^j\left|\widetilde{k}_L^{"j}\right|}}\sin\left[n_h\widetilde{k}_L^j\, r-2\pi n_h j\xi^j\right] \\ &\sim \frac{2}{\pi f\mu_1 r}\sin\left[2\pi fr/\beta_1\right]+\frac{4}{\pi f\mu_1 r}\sum_{j=1}^{j_{\max}}\sqrt{\frac{1}{\left(1+4j^2d^2/r^2\right)}}\sin\left[n_h\widetilde{k}_L^j\, r-2\pi n_h j\xi^j\right], \qquad \text{(C10)}\end{aligned}$$

where $j_{\max} = \text{IntegerPart}[r(2d\beta_1)^{-1}(\beta_2^2-\beta_1^2)^{1/2}]$. Only one half of the contribution of the stationary point ξ^0 can be counted in the first addend of (C10), due to its location just at the lower integration limit ($\xi^0 \to 0$ as $n_h \to \infty$). It is clear from (C10) that, δ_L^- presents, for any *r*, a decreasing amplitude proportional to $1/f$.

ACKNOWLEDGEMENTS

The authors gratefully thank the Editors, Dr. Ludovic Margerin and an anonymous referee for their constructive comments which significantly improved this article. We also thank R. Abreu and M. G. Sánchez for providing useful references. This research was partially supported by the Spanish Comisión Interministerial de Ciencia y Tecnología projects CGL2010-16250 and CGL2011-29499-C02-01, by the European Union with Fondo Europeo de Desarrollo Regional, by DGAPA-UAM under Project IN104712 and the AXA Research Fund. Waveforms obtained from the IU network of the Global Seismic Network (GSN), operated by the USGS Albuquerque Seismological Laboratory have been used in this article. The work done by A. G.-J. was under contract Juan de la Cierva at Instituto Andaluz de Geofísica, Universidad de Granada, Spain.

REFERENCES

Aki, K. (1957), Space and time spectra of stationary stochastic waves, with special reference to microtremors, *Bulletin of the Earthquake Research Institute, 35*, 415–456.

Aki, K., and P. G. Richards (2002), Quantitative Seismology, University Science Books, Sausalito, CA.

Ben-Menahem, A., and S. J. Singh (2000), Seismic waves and sources, 2nd Ed. Dover, New York.

Bettig, B., P.-Y. Bard, F. Scherbaum, J. Riepl, F. Cotton, C. Cornou, and D. Hatzfeld (2001), Analysis of dense array noise measurements using the modified spatial auto-correlation method (SPAC): application to the Grenoble area, *Boll. Geof. Teor. Appl., 42*, 281-304.

Buchen, P. W., and R. Ben-Hador (1996), Free-mode surface-wave computations, *Geophys. J. Int., 124*, 869-887.

Chávez-García, F. J., and F. Luzón (2005), On the correlation of the seismic microtremors, *J. Geophys. Res., 110*, B11313, doi:10.1029/2005JB003671.

De Angelis, S., and P. Bodin (2012), Watching the Wind: Seismic Data Contamination at Long Periods due to Atmospheric Pressure-Field-Induced Tilting, *Bull. Seismol. Soc. Am., 102*, 1255–1265.

Ferrazzini, V., K. Aki, and B. Chouet (1991), Characteristics of seismic waves composing Hawaiian volcanic tremor and gas-piston events observed by a near-source array, *J. Geophys. Res., 96*, 6199-6290.

Forbriger, T. (2007), Low-frequency limit for H/V studies due to tilt, paper presented at 67th Jahrestagung der Deutschen Geophysikalischen Gesellschaft, DGG, Aachen, Germany.

García-Jerez, A., F. Luzón, D. Albarello, E. Lunedei, M. A. Santoyo, L. Margerin, and F. J. Sánchez-Sesma (2012), Comparison between ambient vibrations H/V obtained from the

diffuse field and the distributed surface sources models, paper presented at 15th World Conference on Earthquake Engineering, IAEE, Lisbon, Portugal.

Gilbert, F. (1964), Propagation of transient leaking modes in a stratified elastic waveguide, *Rev. Geophys., 2*, 123-152.

Harkrider, D. G. (1964), Surface waves in multilayered elastic media. Part 1, *Bull. Seismol. Soc. Am., 54*, 627-679.

Harkrider, D. G. (1970), Surface waves in multilayered elastic media. Part II. Higher mode spectra and spectral ratios from point sources in plane layered earth models, *Bull. Seismol. Soc. Am., 60*, 1937-1987.

Haskell, N. A. (1953), The dispersion of surface waves on multilayered media, *Bull. Seismol. Soc. Am., 43*, 17-34.

Hennino, R., N. Trégourès, N. M. Shapiro, L. Margerin, M. Campillo, B. A. van Tiggelen, and R. L. Weaver (2001), Observation of equipartition of seismic waves, *Phys. Rev. Lett., 86*, 3447–3450.

Köhler, A., M. Ohrnberger, F. Scherbaum, M. Wathelet, and C. Cornou (2007), Assessing the reliability of the modified three-component spatial autocorrelation technique, *Geophys. J. Int., 168(2)*, 779-796.

Lin, F. C., M. H. Ritzwoller, and S. Weisen (2011), On the reliability of attenuation measurements from ambient noise cross-correlations, *Geophys. Res. Lett., 38*, L11303.

Luo, Y., Y. Xu, and Y. Yang (2012), Crustal structure beneath the Dabie orogenic belt from ambient noise tomography, *Earth and Planetary Science Letters, 313–314*, 12-22.

Margerin, L. (2009), Generalized eigenfunctions of layered elastic media and application to diffuse fields, *J. Acoust. Soc. Am., 125*, 164–174.

Margerin, L., M. Campillo, B. A. Van Tiggelen, and R. Hennino (2009), Energy partition of seismic coda waves in layered media: theory and application to Pinyon Flats Observatory, *Geophys. J. Int., 177*, 571–585, doi: 10.1111/j.1365-246X.2008.04068.x.

Métaxian, J-P., and P. J. Lesage (1997), Permanent tremor of Masaya Volcano, Nicaragua: Wave field analysis and source location, *J. Geophys. Res., 102*, 22529-22545.

Nakahara, H., and L. Margerin (2011), Testing Equipartition for S-Wave Coda Using Borehole Records of Local Earthquakes, *Bull. Seismol. Soc. Am., 101(5)*, 2243–2251.

Nakamura, Y. (1989), A method for dynamic characteristics estimation of subsurface using microtremor on the ground surface, *Quaterly Rep. Railway Tech. Res. Inst., 30*, 25-30.

Nishida, K., H. Kawakatsu, and K. Obara (2008), Three-dimensional crustal S wave velocity structure in Japan using microseismic data recorded by Hi-net tiltmeters, *J. Geophys. Res., 113*, B10302, doi:10.1029/2007JB005395.

Pawlak, A., D. W. Eaton, I. D. Bastow, J.-M. Kendall, G. Helffrich, J. Wookey, and D. Snyder (2011), Crustal structure beneath Hudson Bay from ambient-noise tomography: implications for basin formation, *Geophys. J. Int., 184*, 65–82.

Pedreira, D., J. A. Pulgar, J. Gallart, and J. Díaz (2003), Seismic evidence of Alpine crustal thickening and wedging from the western Pyrenees to the Cantabrian Mountains (north Iberia), *J. Geophys. Res., 108*, 2204, doi:10.1029/2001JB001667.

Prieto, G. A., J. F. Lawrence, and G. C. Beroza (2009), Anelastic Earth structure from the coherency of the ambient seismic field, *J. Geophys. Res., 114*, B07303, doi:10.1029/2008JB006067.

Reguzzoni, M. and D. Sampietro (2012), Moho estimation using GOCE data: a numerical simulation, in Geodesy for Planet Earth, IAG Symposia, vol. 136, edited by S. Kenyon et al., pp. 205-214, Springer-Verlag, Berlin Heidelberg.

Sánchez-Sesma, F. J. and M. Campillo (2006), Retrieval of the Green's Function from

Cross Correlation: The Canonical Elastic Problem, *Bull. Seismol. Soc. Am., 96(3)*, 1182–1191. doi: 10.1785/0120050181.

Sánchez-Sesma, F. J., J. A. Pérez-Ruiz, M. Campillo, and F. Luzón (2006), The elastodynamic 2D Green function retrieval from cross-correlation: The canonical inclusion problem, *Geophys. Res. Lett*., *33*, L13305, doi:10.1029/2006GL026454.

Sánchez-Sesma, F. J., J. A. Pérez-Ruiz, F. Luzón, M. Campillo, and A. Rodríguez-Castellanos (2008), Diffuse fields in dynamic elasticity, *Wave Motion, 45*, 641–654.

Sánchez-Sesma, F. J., M. Rodríguez, U. Iturrarán-Viveros, F. Luzón, M. Campillo, L. Margerin, A. García-Jerez, M. Suarez, M. A. Santoyo, and A. Rodríguez-Castellanos (2011a), A theory for microtremor H/V spectral ratio: application for a layered medium, *Geophys. J. Int., 186*, 221-225.

Sánchez-Sesma, F. J., R. L. Weaver, H. Kawase, S. Matsushima, F. Luzón, and M. Campillo (2011b), Energy Partitions among Elastic Waves for Dynamic Surface Loads in a Semi-Infinite Solid, *Bull. Seismol. Soc. Am., 101(4),* doi: 10.1785/0120100196.

Shapiro, N. M., and M. Campillo (2004), Emergence of broadband Rayleigh waves from correlations of the ambient seismic noise, *Geophys. Res. Lett., 31*, L07614, doi 10.1029/2004GL019491.

Strollo, A., S. Parolai, K.-H. Jäckel, S. Marzorati, and D. Bindi (2008), Suitability of short-period sensors for retrieving reliable H/V peaks for frequencies less than 1 Hz, *Bull. Seismol. Soc. Am., 98*, 671–681.

Tamura, S. (1996), Comparison of Body and Rayleigh Wave Displacements Generated by a Vertical Force on a Layered Elastic Medium, Proc. 11th World Conf. on Earthquake Engineering. Paper 1722.

Tokimatsu, K. (1997), Geotechnical site characterization using surface waves, Proc. 1st Intl. Conf. Earthquake Geotechnical Engineering, edited by K. Ishihara, pp. 1333-1368, A.A. Balkema, Brookfield, Vt.

Tsai, V. C. (2011), Understanding the amplitudes of noise correlation measurements, *J. Geophys. Res., 116*, B09311.

Wang, C. Y., and R. B. Herrmann (1980), A numerical study of *P*-, *SV*-, and *SH*-wave generation in a plane layered medium, *Bull. Seismol. Soc. Am., 70(4)*, 1015-1036.

Weaver, R. L. (1985), Diffuse elastic waves at a free surface, *J. Acoust. Soc. Am., 78*, 131–136.

Weaver, R. L. (2013), On the retrieval of attenuation and site amplifications from ambient noise on linear arrays: further numerical simulations, *Geophys. J. Int*., doi: 10.1093/gji/ggt063, in press.

Wielandt, E., and T. Forbriger (1999), Near-field seismic displacement and tilt associated with the explosive activity of Stromboli, *Annali di Geofisica, 42*, 407–416.

Yao, H.J., C. Beghein, and R.D. Van Der Hilst (2008), Surface wave array tomography in SE Tibet from ambient seismic noise and two-station analysis – II. Crustal and upper-mantle structure, *Geophys. J. Int., 173*, 205–219.

Yokoi, T., and S. Margaryan (2008), Consistency of the spatial autocorrelation method with seismic interferometry and its consequence, *Geophysical Prospecting, 56*, 435–451.

Ziolkowski, A. (1973), Prediction and suppression of long-period nonpropagating Seismic noise, *Bull. Seismol. Soc. Am., 63(3)*, 937-958.

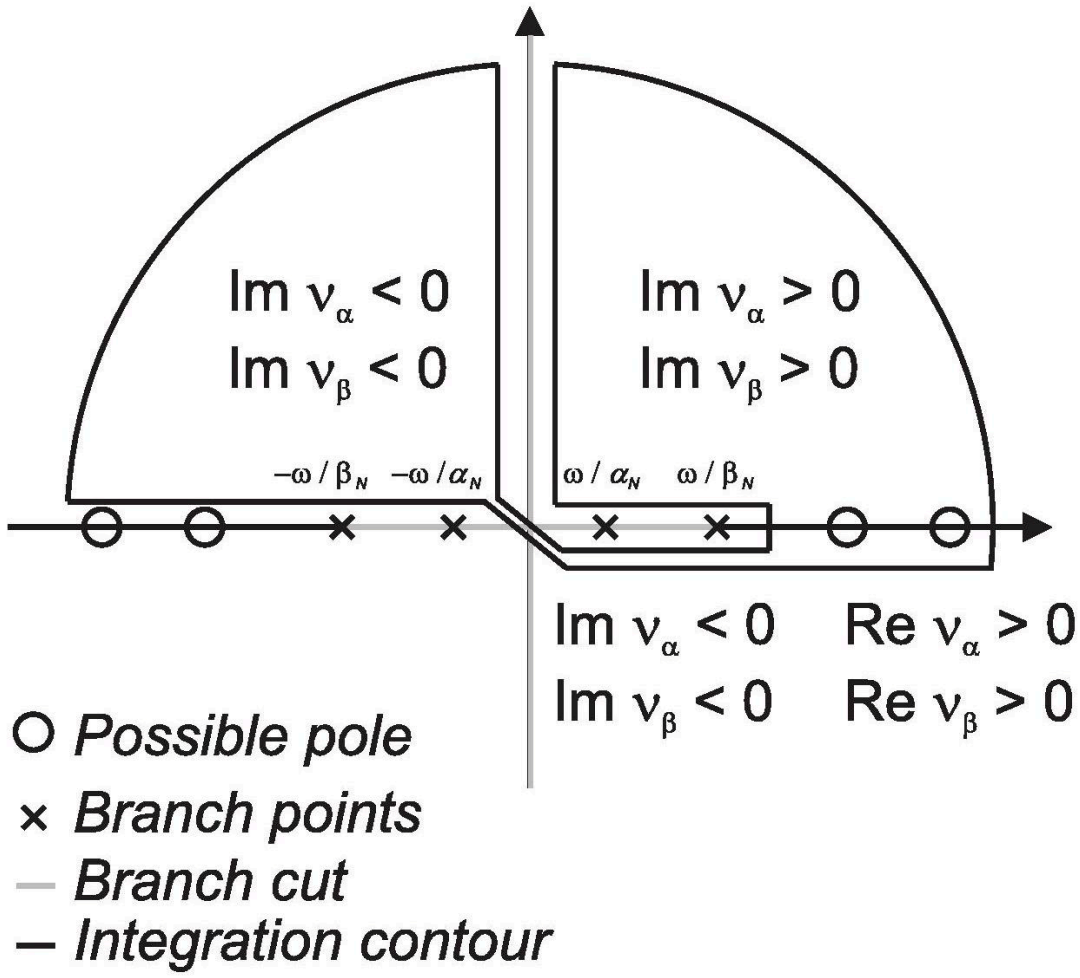

Figure 1. Contour used for complex-plane integration.

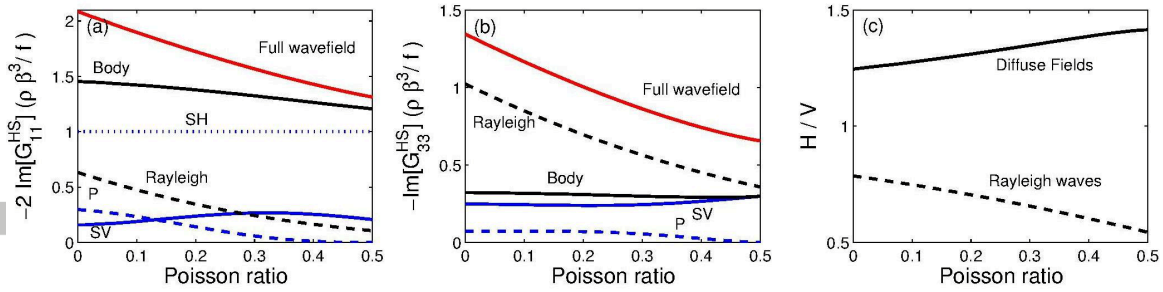

Figure 2. Contribution of the different types of waves to the imaginary part of the halfspace Green's function at a surface source. Note that G_{11}^{HS} (panel a) and G_{33}^{HS} (panel b) are proportional to P_H and P_V, respectively. (c) Horizontal-to-Vertical spectral ratio for the diffuse field. The Rayleigh wave ellipticity is shown for comparison.

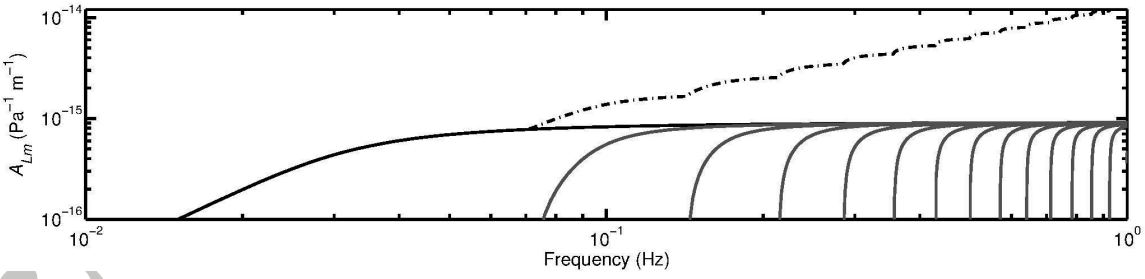

Figure 3. $A_{Lm}(f)$ for the fundamental (black line) and the lower-order higher modes (gray lines) of Model 1 (listed in Table 1). The sum for all the modes is shown with a dot-dashed line.

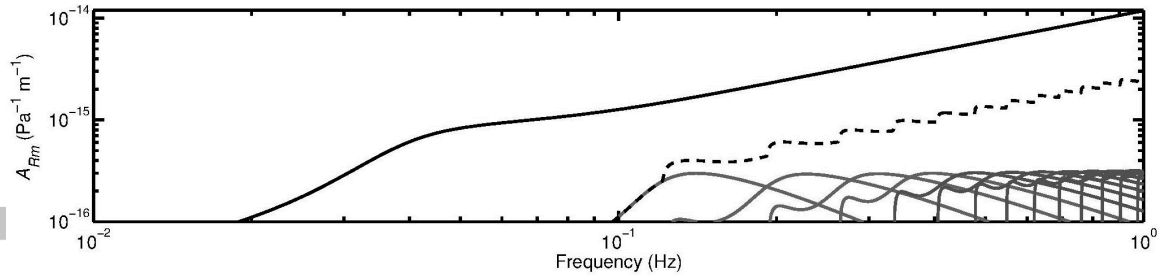

Figure 4. $A_{Rm}(f)$ for the fundamental (solid black line) and lower-order higher modes (gray lines) of Model 1 (Table 1). The sum of higher modes is shown with a dashed black line.

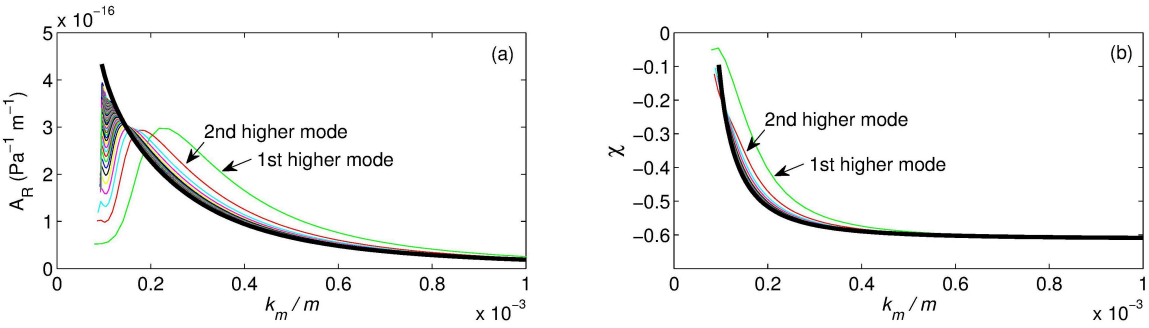

Figure 5. Thin color lines represent the higher-mode medium responses A_{Rm} vs. (k_{Rm}/m) for the 70 lower-order higher modes ($m > 0$). Function $A_{R\infty}(k_{Rm}/m)$ has been shown with thick black line. (b) Respective curves for the higher modes ellipticities χ_m (color) and function $\chi_\infty(k_{Rm}/m)$ (black line). All curves correspond to the crustal Model 1 listed in Table 1.

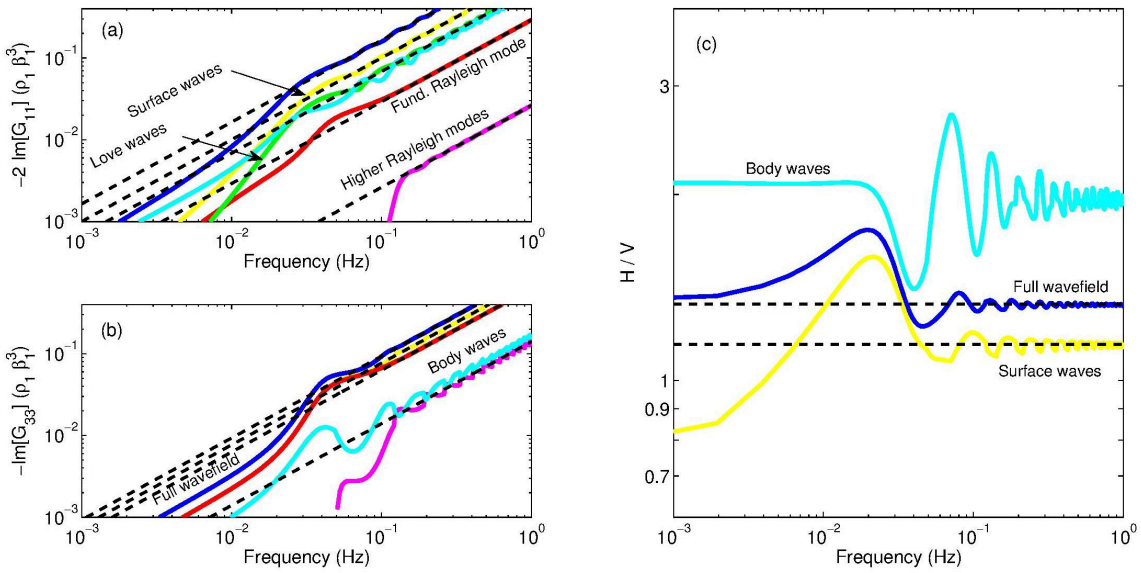

Figure 6. Normalized (a) P_H and (b) P_V calculated from the imaginary parts of $G_{11}(r=0)$ and $G_{33}(r=0)$, Eqs. (8-10). Blue lines represent the FW calculations while yellow and cyan lines represent contributions of SW and BW, respectively, to the quantity shown in each panel. Red, magenta and green lines show contributions of the fundamental Rayleigh mode, all higher Rayleigh modes, and all Love wave modes, respectively. Superimposed dashed lines show their theoretical high-frequency asymptotes, calculated as explained in the main text. (c) Theoretical H/V spectral ratios for FW (blue line), SW (yellow line) and BW (cyan line) and respective high-frequency limits (dashed black lines). All curves correspond to the crustal Model 1 (Table 1).

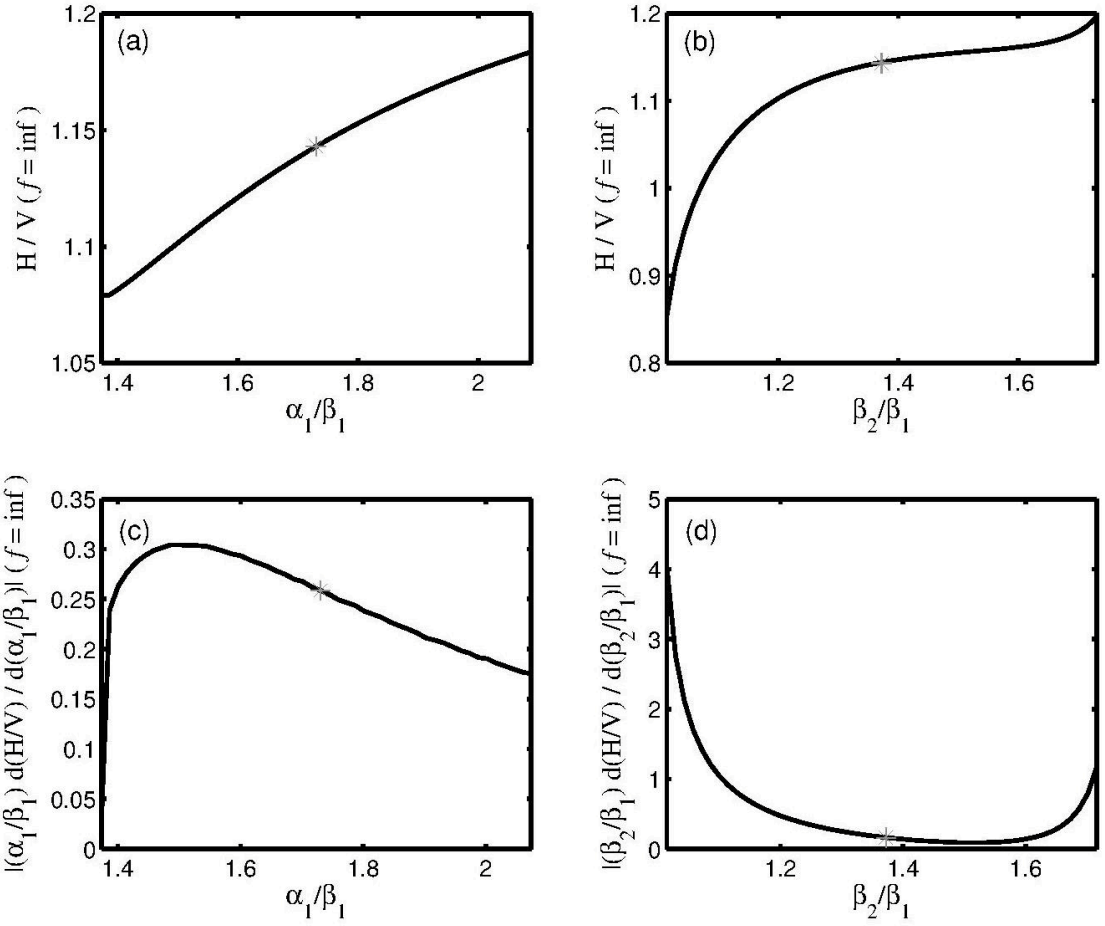

Figure 7. (a) Theoretical high-frequency limit of the $[H/V]_{SW}$ spectral ratio for variations in the upper layer α/β ratio from the crustal Model 1 (Table 1). (b) Similar calculation varying the *S*-wave velocity contrast. (c) $\left|x\,\partial\left[H/V\right]_{SW}/\partial x\right|$ for x representing the *P*- to *S*-wave velocity ratio of the upper layer. (d) Same for x representing the *S*-wave velocity contrast. Points corresponding to the original model are marked with asterisks. Poisson's ratio of the halfspace and density contrast have been kept unaltered.

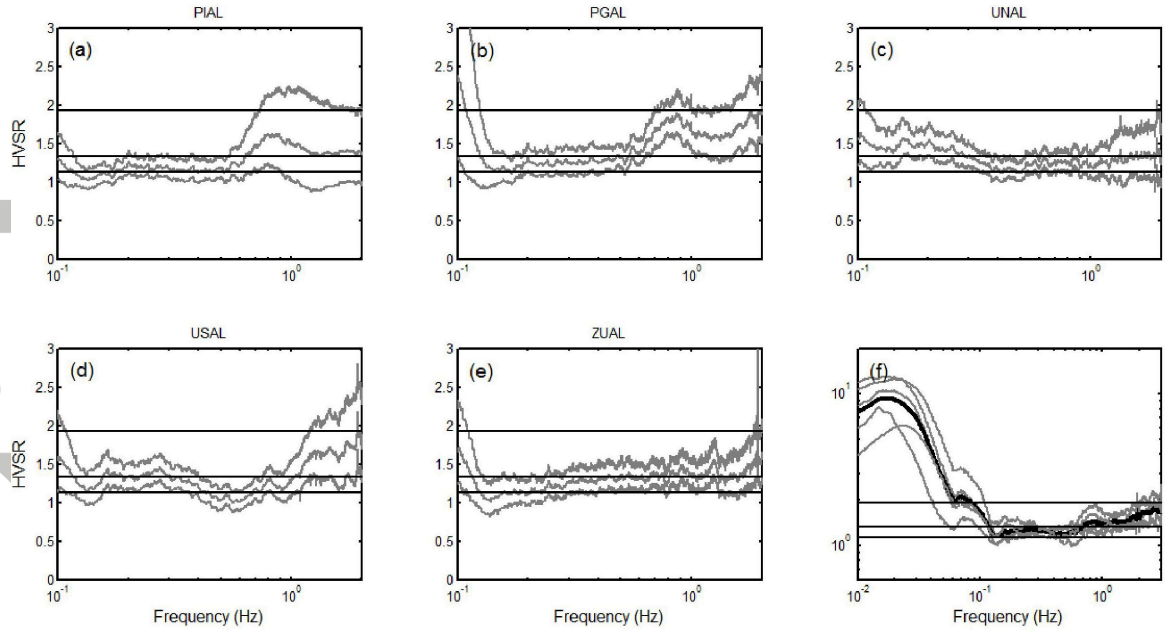

Figure 8. (a-e) Experimental H/V spectral ratio in the band 0.1 - 2 Hz for an array of stations deployed in the western Pyrenean edge. The average curve and the ± 1 standard deviation band are shown with gray lines. (f) H/V spectral ratios for each site (gray lines) and average curve (thick dotted line) shown in a broader frequency range, with a logarithmic scale on both axes. Solid black line (HVSR=1.33) shows the theoretical high-frequency limit of FW-H/V for Model 2 (Table 1) under the DFA, while dashed black line and thin dotted black line correspond to SW-H/V (1.13) and BW-H/V (1.93), respectively.

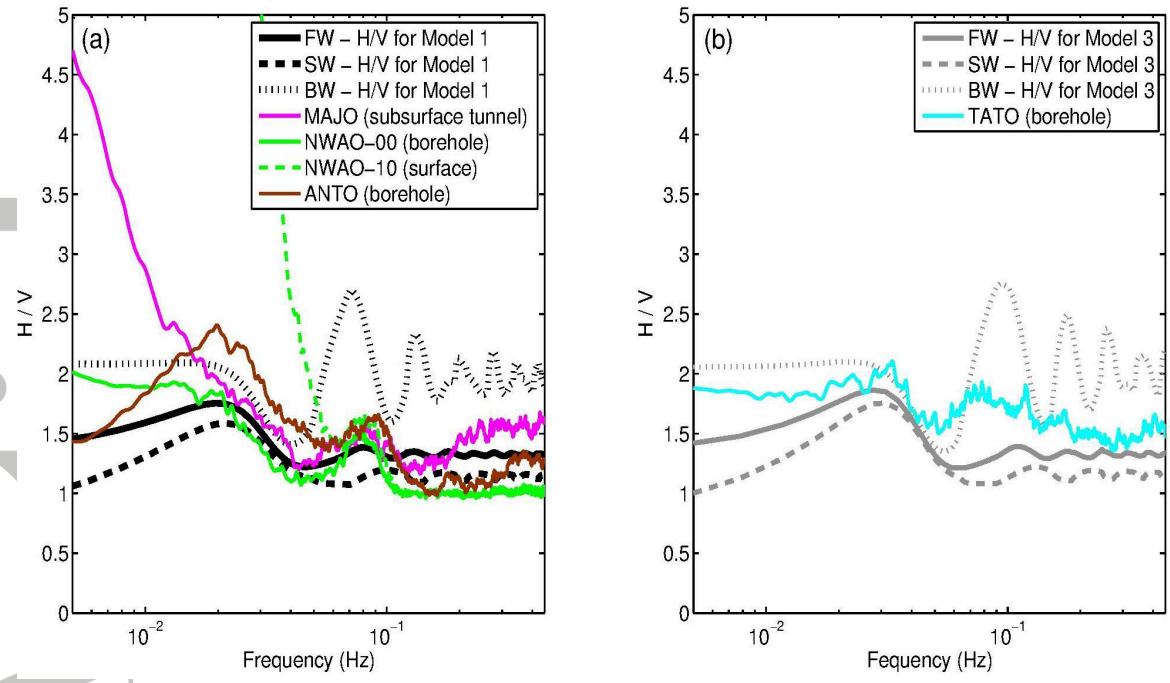

Figure 9. Experimental H/V spectral ratios for some stations of the GSN installed in boreholes or tunnels. (a) Results for stations MAJO (Matsushiro, Japan), NWAO (Narrogin, Australia) and ANTO (Ankara, Turkey) compared with theoretical FW-, SW- and BW-H/V ratios for Model 1 (Table 1) under DFA. (b) Results for station TATO (Taipei, Taiwan) compared with those of a model with thinner crust (Model 3, Table 1). The depths of Moho discontinuity at the station locations obtained from GOCE gravity satellite data (available at http://gocedata.como.polimi.it/) are 34, 39, 37 and 24 km, respectively.

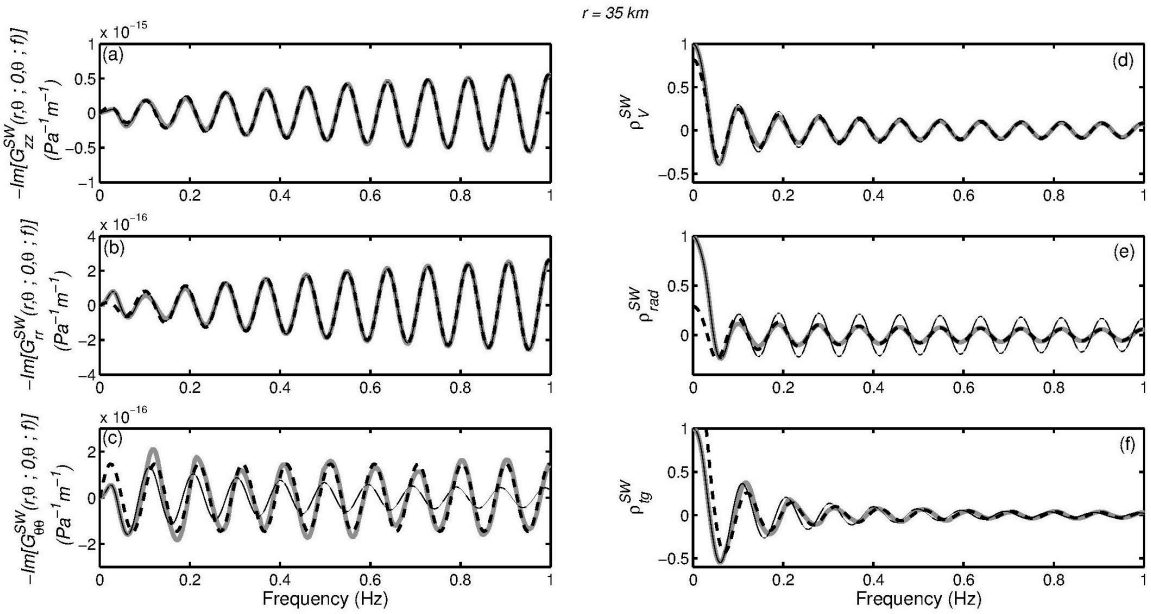

Figure 10. Left hand column: SW-Green's tensor components between surface stations, being proportional to the cross-correlations of their (a) vertical components (b) radial components (c) tangential components. The proportionality factor is $2\pi\omega^{-1}\rho_2\beta_2^3 S^2$. Right hand column: respective Aki's SPAC coefficients for SW under the DFA. In all panels, Gray lines involve exact calculations for all the existing SW modes, while solid black lines result from the restriction to fundamental modes. Dashed black lines in panels (a-c) represent the predicted asymptotic forms, which essentially account for fundamental-mode Rayleigh waves (panels a and b) or constructive actions of Love wave modes (panel c). The corresponding asymptotic forms of the SPAC coefficients (coherences) have been shown with dashed black line in panels (d-e). All these results correspond to the Model 1 (Table 1) and r = 35 km.

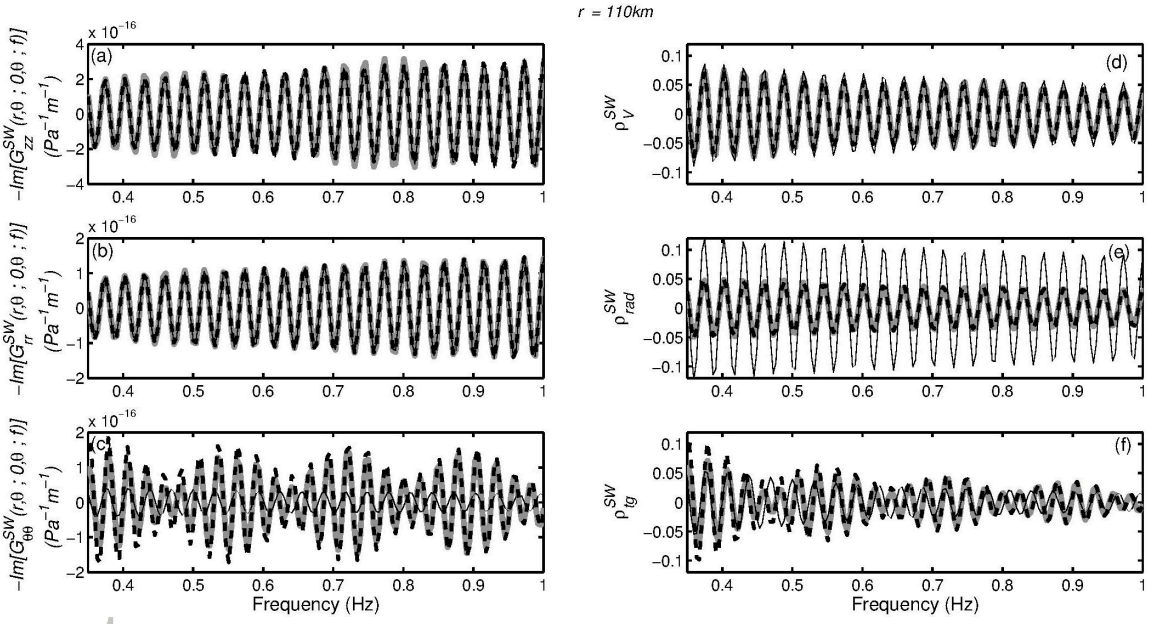

Figure 11. Same as Fig. 10 but for an interstation distance r = 110 km. In this case, ρ_{tg}^{SW} presents two significant stationary-phase contributions and have to be computed taking into account the general expressions derived in Appendix C instead of using Eq. (30).

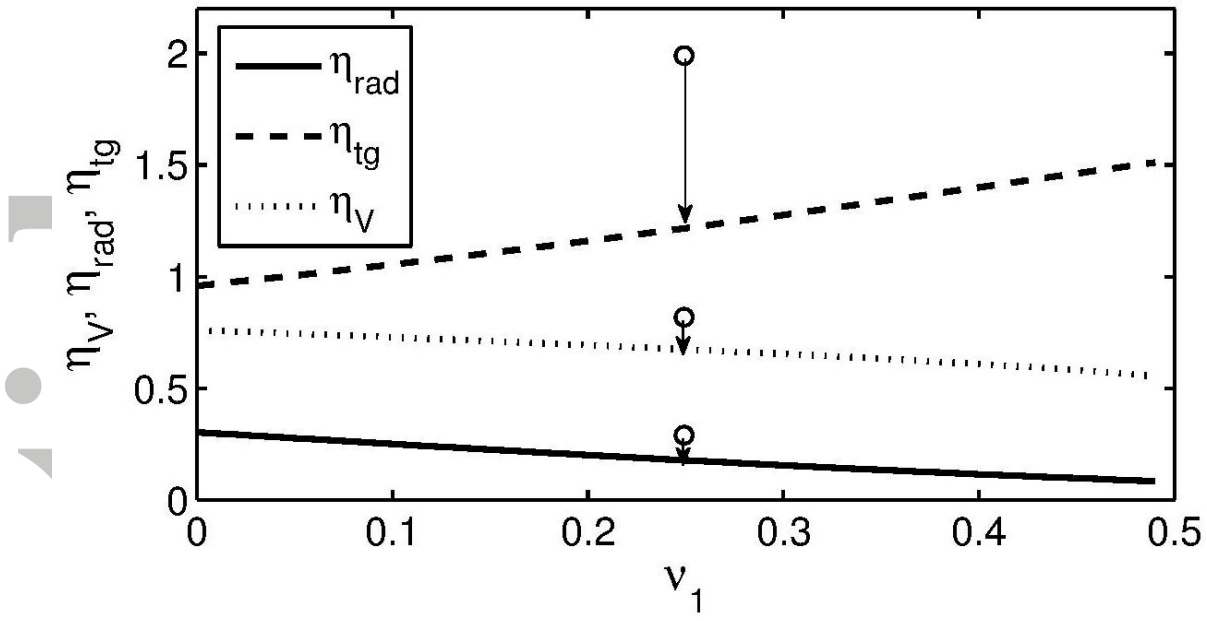

Figure 12. Coefficients η_V, η_{rad} and η_{tg}, accounting for FW, as a function of the upper layer Poisson's ratio. Circles represent SW computations for the model in Table 1.

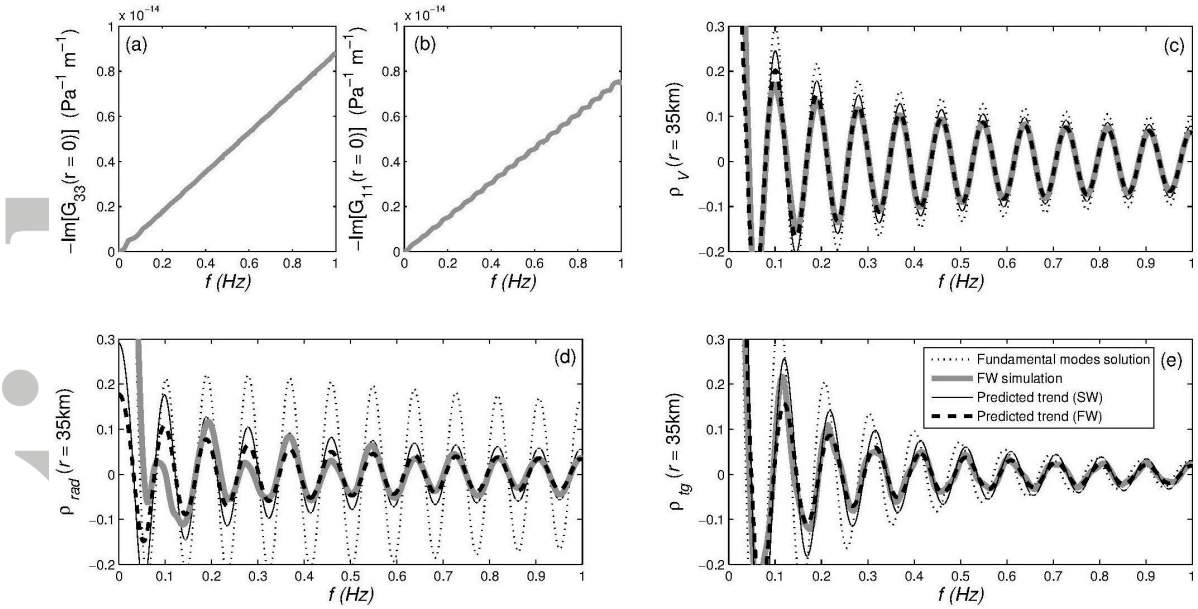

Figure 13. Panels (a) and (b) show the imaginary part of G_{33} and G_{11} at source for FW computation, being proportional to P_V and P_H, respectively. Panels (c), (d) and (e) show FW-SPAC coefficients (thick gray lines) under DFA compared with the derived asymptotic expressions (dashed black lines, obtained from Eqs. (28), (29) and (30) by using the FW values of η_V, η_{rad} and η_{tg}: 0.67, 0.18 and 1.22). The asymptotic trend of the SW components (thin black line) and the exact solution for fundamental modes (dotted black line) have been presented for reference. All calculations correspond to the Model 1 and r = 35 km.

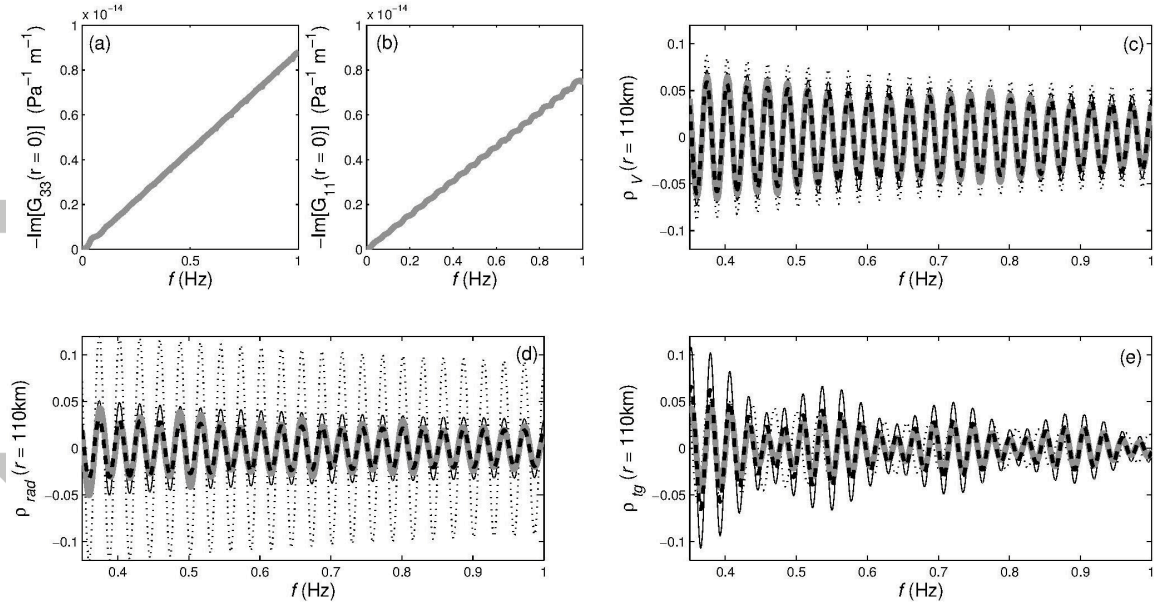

Figure 14. Same as Fig. 13 but for an interstation distance of r = 110 km. As in Fig. 11f, ρ_{tg}^{SW} have to be computed on the basis of Eq. (C10).

Table 1. Simple continental waveguide models.

d (km)	α (km/s)	β (km/s)	ρ (g/cm^3)
Model 1. Generic continental crust model[a]			
35	5.9	3.41	2.67
∞	8.1	4.68	3.27
Model 2. Simple crustal model for the array site[b]			
46.8	6.20	3.61	2.72
∞	8.20	4.73	3.89
Model 3. Simple crustal model for site TATO			
24	5.68	3.20	2.67
∞	8.20	4.73	3.89

[a] Taken from *Gilbert* [1964].

[b] Synthetized taking into account *Pedreira et al.* [2003].

Table 2. Coordinates of the stations.

Station	Latitude N (º)	Longitude W (º)	Elevation (m)
UNAL	42.7560	1.4989	704
USAL	42.9469	1.5478	813
ZUAL	42.8610	1.4565	646
PIAL	42.8049	1.3543	746
PGAL	42.8035	1.3586	588